This is a peer-reviewed, accepted author manuscript of the following research article: Cai, Y, Zhao, H, Li, X, Shi, W & Xiao, Q 2025, 'Developing an OpenFOAM solver for coupled aero-hydrodynamic analysis of integrated structure with floating offshore wind turbine and aquaculture net cage', Coastal Engineering, vol. 198, 104720. https://doi.org/10.1016/j.coastaleng.2025.104720

Developing an OpenFOAM solver for coupled aero-hydrodynamic analysis of integrated structure with floating offshore wind turbine and aquaculture net cage

Yefeng Cai[1,2,4], Haisheng Zhao[1,2,4,*], Xin Li[1,2,4], Wei Shi[1,3,4], Qing Xiao[5]

[1] State Key Laboratory of Coastal and Offshore Engineering, Dalian University of Technology, Dalian 116024, China
[2] School of Infrastructure Engineering, Dalian University of Technology, Dalian, 116024, China
[3] Deepwater Engineering Research Centre, Dalian University of Technology, Dalian, 116024, China
[4] NingBo Institute of Dalian University of Technology, Ningbo 315032, China
[5] Department of Naval Architecture, Ocean and Marine Engineering, University of Strathclyde, Glasgow, UK
[*] Corresponding author. E-mail: hzhao@dlut.edu.cn (H. Zhao)

Abstract

The integrated structure of floating offshore wind turbines (FOWTs) and aquaculture net cages has garnered significant attention in recent years. This study establishes, for the first time, a CFD analysis method for the integrated structure of FOWTs and aquaculture cages, and develops a specialized solver, HybridMarineFoam, for coupled analysis of the integrated structure. The solver currently includes aerodynamic, hydrodynamic, mooring, and aquaculture cage computation modules. The aquaculture cage module is based on the Darcy-Forchheimer model, incorporating the influence of the floating platform's motion into the Darcy-Forchheimer equation and accounting for the hydrodynamic impact of the cage on the floating platform, thus achieving coupled calculations between the fish cage and the floating platform. In this study, the force loading calculation for the moving aquaculture cage and the coupling simulation for the integrated structure have been very well validated. Subsequently, an integrated structure,

combining an IEA 15 MW FOWT and an aquaculture cage, was proposed, and the HybridMarineFoam solver was used to analyze its aerodynamic, hydrodynamic, and flow field characteristics under different wind speeds, wave heights and water current speeds. The results reveal that the presence of the cage significantly impacts the system dynamics motion response and flow field characteristics of the floating wind turbine.

Keywords: Floating offshore wind turbine; Aquaculture net cage; OpenFOAM; Multi-purpose platform; Flow field

1. Introduction

With the increasing global demand for clean energy, floating offshore wind turbines (FOWTs) have become a crucial option for addressing energy crises and environmental issues (Cai et al., 2023a; Lykke Andersen et al., 2011; Myrhaug and Holmedal, 2010; Wang et al., 2024; Zhang et al., 2024). Its deployment in the ocean not only enables the effective utilization of offshore wind energy resources but also avoids the occupation of land resources, which is of great significance in promoting marine economy and environmental protection. However, FOWTs face several practical challenges. One significant challenge is economic feasibility, encompassing factors such as equipment and operational costs, necessitating the development of cost-reducing technologies and strategies. To tackle these challenges, researchers have recently begun exploring the integration of floating wind power with aquaculture net cages. This multi-purpose offshore floating structure offers distinct advantages over conventional systems. Compared to standalone FOWTs, the integrated structure can generate greater economic benefits and improve the efficiency of offshore space utilization. Compared

to traditional aquaculture net cages, the integrated structure allows aquaculture facilities to leverage the wind turbine platform and mooring system, significantly reducing construction and installation resources. Moreover, the wind turbine structure provides a stable energy supply for aquaculture operations, such as powering water quality monitoring and automated feeding systems, enhancing the sustainability of aquaculture. These interactions between wind power and aquaculture not only optimize marine space usage but also promote economic and environmental sustainability, addressing the increasing global demand for efficient and sustainable offshore solutions.

In the context of renewable energy and sustainable development, the combination of offshore wind energy and marine aquaculture has emerged as an innovative solution. Compared to traditional nearshore aquaculture, deep-sea aquaculture faces more complex environmental conditions. The feasibility of integrating floating offshore wind turbines (FOWTs) with aquaculture cages is still being explored, and the interaction mechanisms between these two structures are not yet fully understood. Preliminary studies have utilized experimental methods to investigate the dynamic characteristics of these integrated systems. For example, an integrated model combining a semi-submersible wind turbine with an aquaculture cage was tested at a 1:40 scale, revealing that the net provided a damping effect on the system's dynamics (Cao et al., 2022). Another study developed an integrated structure combining a floating wind turbine, aquaculture cage, and wave energy device, with 1:40 scale model experiments showing that the aquaculture cage suppressed structural motion under irregular wave conditions (Yi et al., 2024). Further research involving a combined semi-submersible wind turbine

and aquaculture cage structure, using both experimental and numerical simulation methods, demonstrated that the presence of the cage increased the average surge response while reducing the pitch motion response (Chen et al., 2024).

Numerous studies have experimentally investigated the mechanical properties of plane nets and net cage structures under various conditions, leading to the development of multiple empirical formulas for calculating loads on cage structures. However, accurately simulating the loads on the overall cage structure in waves and currents remains challenging in numerical simulations. Researchers have explored the integration of FOWTs with aquaculture cages using various simulation tools. One study used OrcaFlex software to model an integrated structure where net loads were calculated using the Morison method (Lei et al., 2020). This study found that the net enhances overall structural damping and reduces the motion response amplitude operators (RAOs) when the wave period aligns closely with the structure's natural period. However, this damping effect is minimal when the wave period differs significantly from the natural period. Another study introduced a novel integrated structure featuring a barge-type wind turbine and aquaculture cage, analyzing its dynamic response to wind, waves, and currents using SESAM software (Zhai et al., 2022; Zhai et al., 2024). This analysis concluded that the net reduced the motion response amplitude and improved overall stability. Additionally, another innovative FOWT-aquaculture cage structure was proposed and examined using FAST and AQWA software, establishing a fully coupled dynamic model to analyze the system's dynamic response (Zhang et al., 2022).

Common methods, such as the Morison method (Dong et al., 2020; Kristiansen and Faltinsen, 2015; Shen et al., 2018) and the screen model method (Huang et al., 2007; Huang et al., 2008), enable quick and accurate calculations of loads acting on the net but fail to capture the net's impact on the flow field. Additionally, these methods are based on potential flow theory, which does not account for fluid viscosity effects. To address this limitation, Patursson et al., (2010) proposed a CFD-based approach utilizing a porous media model to simulate net cages, facilitating the analysis of both the loads on the net cage and its effect on the flow field. Subsequent studies employed this model to investigate the influence of net angles, cage spacing, and the effects of marine biofouling on wave attenuation (Zhao et al., 2013; Bui et al., 2020). Additionally, research into different array configurations of spherical cages revealed that staggered arrays reduce flow obstruction and biofouling (Bi et al., 2017).

Given the advantages of CFD methods in accurately simulating flow fields, these techniques have also been widely applied to the modeling of FOWTs. Being complex systems subjected to various environmental loads—such as aerodynamic forces, hydrodynamic forces, and mooring line loads—FOWTs have garnered significant attention in recent years. Researchers have investigated the dynamic characteristics of FOWT through CFD simulations (Cai et al., 2023b; Limacher, 2022; Mao and Sørensen, 2018). A fully coupled CFD simulation model for a tension-leg platform (TLP) FOWT was developed and validated against experimental data, demonstrating accurate rotor thrust results and minor discrepancies in platform motion response (Ren et al., 2014). Another study used overset grid technology to model a 5 MW semi-submersible FOWT,

analyzing changes in aerodynamic thrust, motion response, mooring line loads, and near-wake dynamics (Tran and Kim, 2016; Tran and Kim, 2018). A fully coupled FOWT model was also developed using OpenFOAM (Jasak, 1996), examining aerodynamic and hydrodynamic characteristics under varying wind speeds and wave heights (Liu et al., 2017). Furthermore, research has investigated the impact of different environmental loads, such as focused waves and turbulent inflows, on the dynamic behavior of FOWTs (Zhou et al., 2019; Zhou et al., 2022; Zhou et al., 2021). The actuating line model (Li et al., 2022; Sørensen and Shen, 2002; Wang et al., 2023) (ALM) is a widely used method for simulating blades in CFD simulations. It calculates loads based on Blade Element Moment (BEM) theory and projects these loads onto the flow field. Although less accurate than real blade models, ALM is preferred for its computational efficiency. Many researchers have developed FOWT solvers using ALM. One study integrated ALM into a multiphase flow solver to analyze the motion response and wake characteristics of the OC3-Hywind floating wind turbine (Huang et al., 2019). Another advanced this work by modeling the NREL 5 MW semi-submersible wind turbine with overset grid techniques, focusing on aerodynamic loads' impact on hydrodynamics (Cheng et al., 2019). Additional research developed a solver named turbinesFoam to simulate fixed wind turbines' aerodynamic characteristics and wake. This solver was later enhanced to include six-degree-of-freedom data for floating structures, creating a coupled model for FOWTs (Pericàs, 2022). Furthermore, a fully coupled solver, qaleFOAM-BM, was developed, incorporating blade elasticity to extend ALM's applicability (Yu et al., 2023).

Although CFD methods have been widely applied to the simulation of individual wind turbines and net cages, a few researchers have also utilized CFD for studying the integration of fixed wind turbines and aquaculture net cages (Wang et al., 2023; Zhao et al., 2023; Zhu et al., 2022). However, to date, there has been no research using CFD methods for the integration of floating wind turbines and aquaculture net cages. Considering the aerodynamic, hydrodynamic and flow field characteristics of integrated structures with the FOWT and aquaculture net cage using CFD methods remains a significant challenge due to the absence of coupling motion module in most commercial CFD software. Herein, we developed a CFD-based coupling solver for FOWTs and aquaculture net cages to bridge this gap in the framework of open-source software OpenFOAM. In this paper, the modeling and simulation methods are detailed in Section 2. Section 3 outlines the coupling process of the developed solver. Section 4 describes the validation procedures for both the net and the FOWT. The application of the solver is presented in Section 5.

2. Numerical methods

2.1. Governing equations

For transient, incompressible, and viscous fluid, the Reynolds-Averaged Navier Stokes (RANS) equations are defined as follows:

$$\frac{\partial u_i}{\partial x_i} = 0 \tag{1}$$

$$\frac{\partial \rho u_i}{\partial t} + \frac{\partial}{\partial x_j}\left(\rho u_j u_i\right) = f_i - \frac{\partial p^*}{\partial x_i} + \frac{\partial}{\partial x_j}\left[\mu_{eff}\frac{\partial u_i}{\partial x_j}\right] \tag{2}$$

where $\rho$is the fluid density; p^* is the pressure by subtracting the hydrostatic part

from total pressure p; $\mu_{eff} = \rho(\nu + \nu_t)$ is effective dynamic viscosity, in which ν and ν_t are the kinematic and eddy viscosity respectively; f_i is an external body force including gravity.

The $k-\omega$ SST Buoyancy turbulence model (Devolder et al., 2017, 2018) is adopted to prevent excessive turbulence at the two-phase flow interface, which can lead to wave height attenuation. The governing equations are:

$$\frac{\partial \rho k}{\partial t} + \frac{\partial \rho u_j k}{\partial x_j} - \frac{\partial}{\partial x_j}\left[\rho(\nu + \sigma_k \nu_t)\frac{\partial k}{\partial x_j}\right] = \rho P_k - \rho\beta^* \omega k + G_b \tag{3}$$

$$\begin{aligned} &\frac{\partial \rho \omega}{\partial t} + \frac{\partial \rho u_j \omega}{\partial x_j} - \frac{\partial}{\partial x_j}[\rho(\nu + \sigma_\omega \nu_t)\frac{\partial \omega}{\partial x_j}] \\ &= \frac{\gamma}{\nu_t}\rho G - \rho\beta\omega^2 - 2(F_1 - 1)\rho\sigma_{\omega 2}\frac{1}{\omega}\frac{\partial k}{\partial x_j}\frac{\partial \omega}{\partial x_j} \end{aligned} \tag{4}$$

$$G_b = -\frac{\upsilon_t}{\sigma_t}\frac{\partial \rho}{\partial x_j} g_j \tag{5}$$

where k is the turbulence kinetic energy, P_k is the production term of k, ω is the specific dissipation rate. The buoyancy term G_b is treated implicitly, and the scalar σ_t = 0.85 and vector $g = [0, 0, -9.81]\mathrm{m/s^2}$.

2.2 Free surface capturing

The local density ρ and the effective dynamic viscosity μ_{eff} are defined by the volume fraction α, where $\alpha = 0$ denotes air phase, $\alpha = 1$ denotes water phase and $0 < \alpha < 0$ represents free surface. The volume fraction α is governed by the following equation:

$$\frac{\partial \alpha}{\partial t} + \frac{\partial u_i \alpha}{\partial x_i} + \frac{\partial u_{r,i}\alpha(1-\alpha)}{\partial x_i} = 0 \tag{6}$$

where u_r is an artificial velocity field suitable to compress the interface. For two phase

flow simulation, fluid properties are calculated as weighted averaging based on the volume fraction of water and air as follows:

$$\rho = \alpha\rho_{water} + (1-\alpha)\rho_{air} \quad (7)$$

$$\mu_{eff} = \alpha\mu_{water} + (1-\alpha)\mu_{air} \quad (8)$$

2.3 Actuator line model

Utilizing body forces to simulate the impact of blades on the flow field, the ALM efficiently lowers computational costs by replacing the physical blade surfaces with virtual actuator lines, eliminating the need to resolve the detailed blade geometry. In ALM, the blade is divided into several blade elements along the radial direction, and the lift and drag forces for each blade element are calculated using the following formula:

$$L = \frac{1}{2}C_l(\alpha)\rho_{air}U_{rel}^2 cdr \quad (9)$$

$$D = \frac{1}{2}C_d(\alpha)\rho_{air}U_{rel}^2 cdr \quad (10)$$

where $C_l(\alpha)$ and $C_d(\alpha)$ are the lift and drag coefficients, α is local angle of attack (AOA), ρ_{air} is the air density, U_{rel} represents the relative velocity of the blade section, *c* is the chord length and *dr* represents the width of the blade element. Fig. 1 shows the velocity component of a blade element. According to Fig. 1, the magnitude of U_{rel} can be calculated as:

$$U_{rel} = U_{in} - \Omega \times r + U_{rot} + U_M \quad (11)$$

where U_{in} is the inflow velocity, Ω represents the angular velocity of rotation, r represents the length from the blade element to the rotation center, U_{rot} is the component of the inflow velocity in the rotor plane, U_M is the velocity induced by the platform motion. The following Gaussian weight function adopted by Sørensen and Shen (Sørensen and Shen, 2002) was used to project the actuator force to the

computational domain:

$$\eta_\varepsilon(d) = \frac{1}{\varepsilon^3 \pi^{3/2}} exp\left[-\left(\frac{d}{\varepsilon}\right)^2\right] \tag{12}$$

The body force at (x, y, z) in the flow field can be calculated as:

$$f_\varepsilon(x,y,z,t) = f \otimes \eta_\varepsilon = \sum_{j=1}^{N} f(x_i, y_i, z_i, t) \frac{1}{\varepsilon^3 \pi^{3/2}} exp\left[-\left(\frac{d_i}{\varepsilon}\right)^2\right] \tag{13}$$

where (x_i, y_i, z_i) is the actuator point, d_i is the distance between the point (x, y, z) and the point (x_i, y_i, z_i), ε is the Gaussian smoothing parameter.

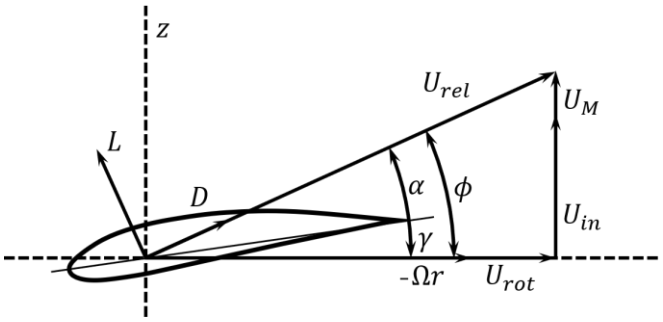

Fig. 1. Velocity component on blade section.

2.4 Wave generation and absorption

Numerical waves are generated using the open-source toolbox "waves2Foam" (Jacobsen et al., 2012) at the inlet boundary and absorbed at the outlet boundary in a designated numerical wave tank. Explicit relaxation zones have been implemented to prevent reflection of waves from outlet boundaries and further to avoid waves reflected internally in the computational domain to interface with the wave-maker boundary:

$$\varphi = \alpha_R \varphi_{computed} + (1 - \alpha_R)\varphi_{target} \tag{14}$$

where φ is either the velocity or volume fraction α. φ_{target} is the quantities given by wave theories while $\varphi_{computed}$ is the computed velocity. α_R is the relaxation function defined as:

$$\alpha_R(\chi_R) = 1 - \frac{\exp\left(\chi_R^{3.5} - 1\right)}{\exp(1) - 1} \tag{15}$$

where χ_R is between 0 and 1. In this study, the stokes second order regular wave theory is adopted to simulate waves. The wave surface equation describes the position of the wave surface as it varies with time and space. For stokes second order waves, the velocity potential function and wave surface function can be expressed as:

$$\phi = \frac{\pi H}{kT}\frac{cosh\, k(z+h)}{\sinh \mathrm{kh}}\sin\theta + \frac{3}{8}\frac{\pi^2 H}{kT}\left(\frac{H}{L}\right)\frac{\cosh 2k(z+h)}{\sinh^4 kh}\sin 2\theta \tag{16}$$

$$\eta = \frac{H}{2}\left[cos\,\theta + \frac{Hk}{8}\,\frac{\cosh(kh)\cdot(\cosh(2kh)+2)}{\sinh^3 kh}\cos 2\theta\right] \tag{17}$$

$$\theta = kx - \omega t \tag{18}$$

where H is the wave hight, $k = 2\pi/L$ is the wave number, ω is the angular frequency, L is the wave length, h represents the water depth.

2.5 Mooring line system

In this study, the MoorDyn toolbox, which employs the lumped mass method, was used to simulate the mooring line dynamics. Chen and Hall (2022) integrated MoorDyn with OpenFOAM to simulate the mooring dynamics of floating structures. In the lumped mass method, the mooring line is divided into n+1 concentrated mass points, connected by massless springs (Fig. 2). The Morison equation is used to calculate the hydrodynamic loads on the mooring line. The equations of motion for the mooring line are solved by accounting for gravity, buoyancy, seabed contact forces, and the internal stiffness and damping of the mooring line:

$$(m_i\mathbf{I}+\mathbf{a}_i)\ddot{\mathbf{r}}_i=\mathbf{T}_{i+\frac{1}{2}}-\mathbf{T}_{i-\frac{1}{2}}+\mathbf{C}_{i+\frac{1}{2}}-\mathbf{C}_{i-\frac{1}{2}}+\mathbf{W}_i+\mathbf{B}_i+\mathbf{D}_{ni}+\mathbf{D}_{ti} \tag{19}$$

where m_i is the mass of the lumped mass point, $\mathbf{a}_i$ is the added mass matrix, $\ddot{\mathbf{r}}_i$ is the acceleration between fluid and mooring node, **T** and **C** are the mooring line tension and internal damping force of the adjacent node. $\mathbf{W}_i$ is the buoyancy of node *i*, $\mathbf{B}_i$ is the vertical seabed reaction force applied on node. $\mathbf{D}_{ni}$ and $\mathbf{D}_{ti}$ are the transverse and tangential component of drag force.

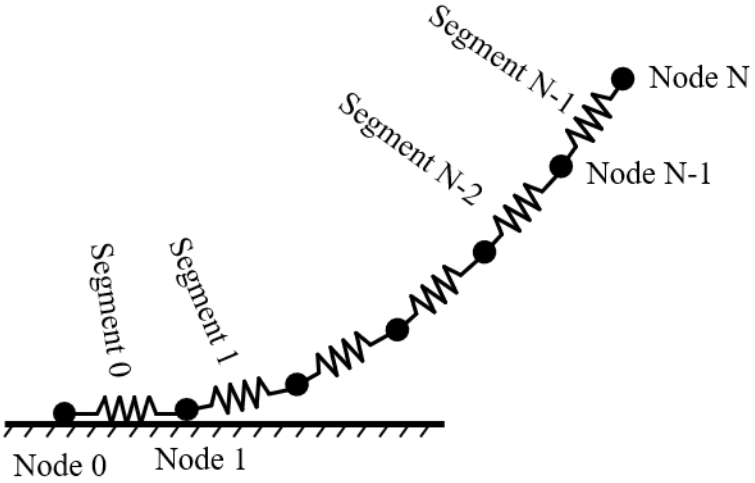

Fig. 2. Sketch of the model for lumped mass method.

3. Development of HybridMarineFoam solver

3.1 Framework of HybridMarineFoam solver

A novel OpenFOAM solver, namely HybridMarineFoam, is developed to simulate the dynamic response of integrated structures of FOWTs and aquaculture cages in complex marine environments, where its overall framework is shown in Fig. 3. The solver is centered on a multi-region coupling method, incorporating condition input as well as aerodynamic, hydrodynamic, mooring, and aquaculture cage core calculation modules. Among these, the modules highlighted with red borders in Fig. 3 are those

developed in this study, which are detailed in the following sections. The solver currently supports multiple environmental load inputs: wind loads include uniform, shear and turbulent winds, while wave loads include regular, focused and solitary waves. Additionally, a wave-current coupling module that considers Doppler effects has been developed within the framework. Wind input is processed in the "Wind turbine region" to generate aerodynamic loads on the blades, calculating the aerodynamic response of the rotor to the overall structure. Wave and current inputs act on the structure through the "Floating platform region", generating hydrodynamic loads, mooring loads, and aquaculture cage loads. These loads are coupled through the self-developed multi-region coupling calculation method within the solver, enabling dynamic response analysis of the FOWT and aquaculture cage integrated structure.

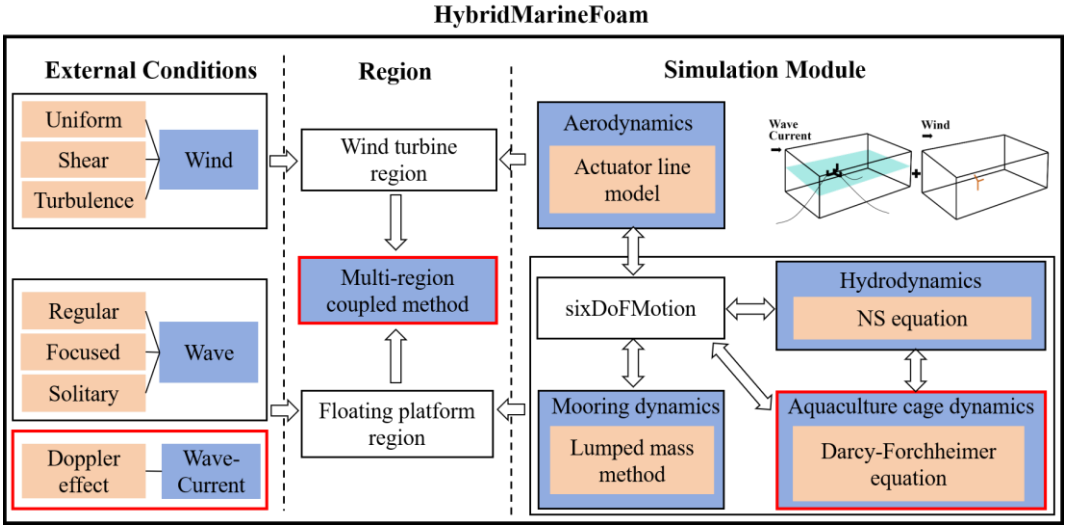

Fig. 3. The framework of HybridMarineFoam solver.

3.2 Multi-region coupled analysis method

In traditional CFD simulations of FOWTs, calculations are typically performed within a unified computational domain. In contrast, HybridMarineFoam separates the domain into two distinct regions: one dedicated to the floating platform and the other

to the wind turbine rotor. This separation enables independent computations of the platform's six degrees of freedom (6-DOF) motion and the aerodynamic forces acting on the rotor, as depicted in Fig. 4. By dividing the computational domain, HybridMarineFoam significantly reduces grid requirements and enhances the overall efficiency of the simulation process.

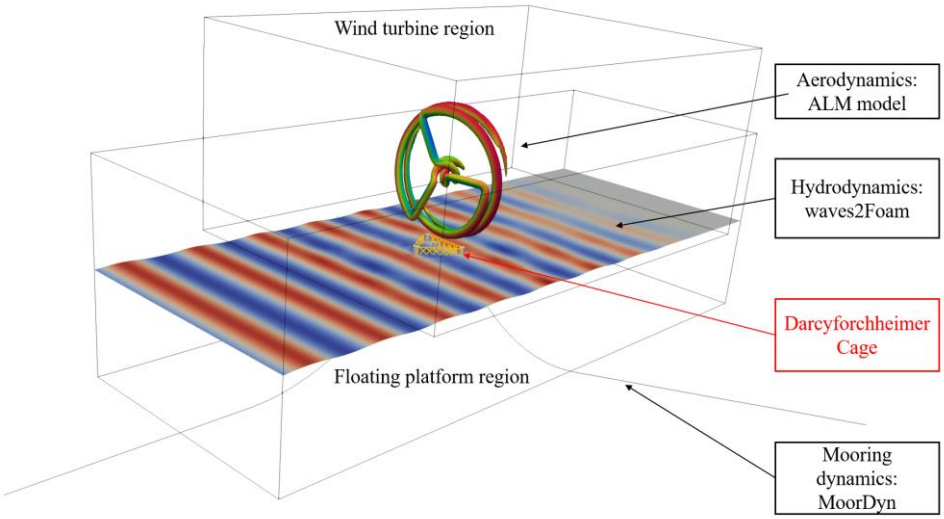

Fig. 4. Sketch of multi region solver – HybridMarineFoam.

The overall workflow of the HybridMarineFoam solver is shown in Fig. 5, while Fig. 6 provides a detailed representation of the interaction between the two computational regions. In the initial time step, surface forces on the floating platform are calculated using the initialized flow field, which are then applied to determine the platform's 6-DOF motion response. Using this motion, the loads on the mooring lines are subsequently computed. The platform's motion is then transferred to the wind turbine domain to influence the calculation of aerodynamic loads on the rotor (as shown in Step 1 of Fig. 6). In the next time step, the aerodynamic loads obtained from the prior step are used to update the platform's motion for the current step (Step 2 in Fig. 6). This

process iteratively exchanges data between the platform's motion and the rotor's aerodynamic loads, enabling a dynamic and efficient simulation of the coupled FOWT system until completion, where its accuracy and efficiency will be verified in Section 4.2.

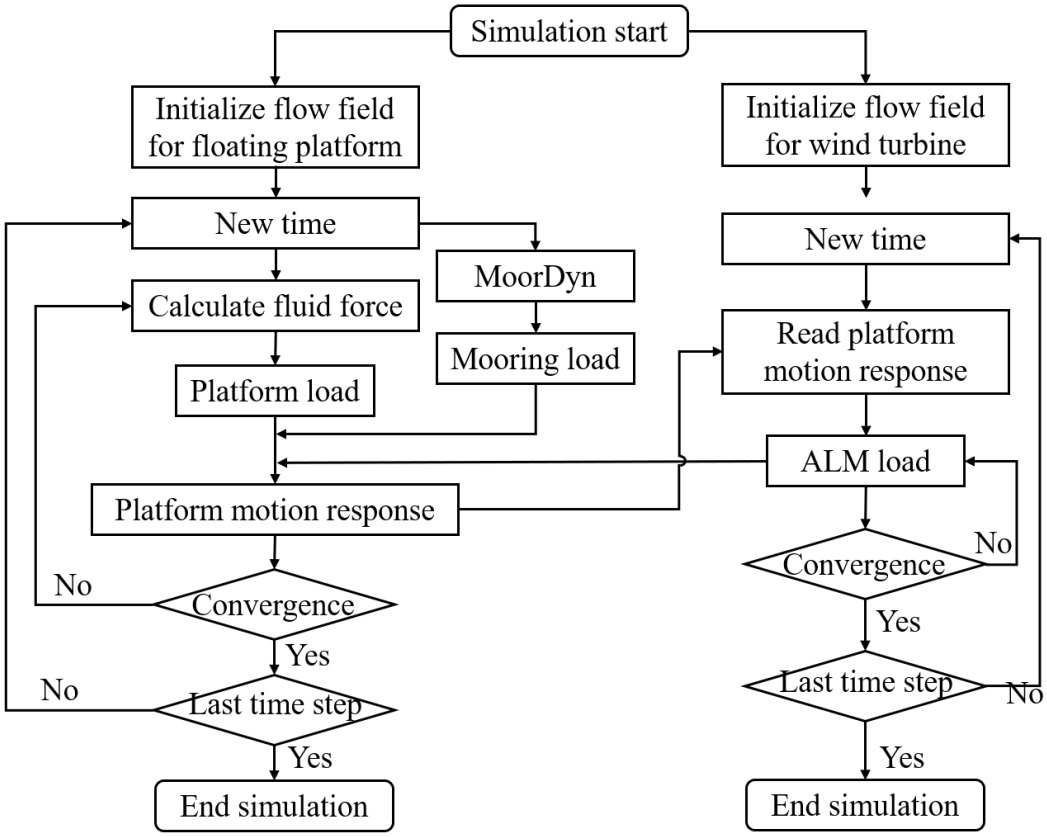

Fig. 5. Flow chart of the multi-region coupled method.

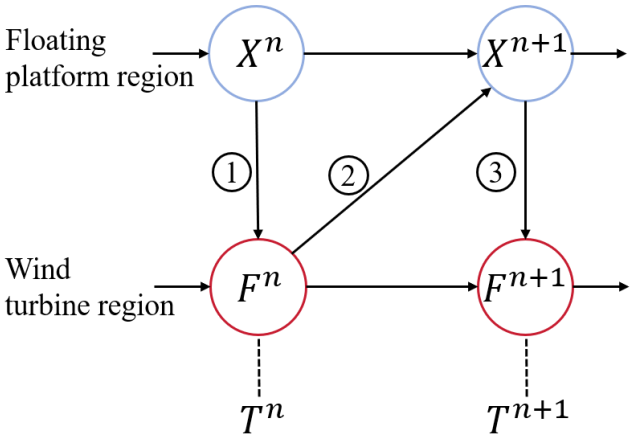

Fig. 6. Coupling approach of computational region of HybridMarineFoam solver.

3.3 Coupled FOWT-cage computation module

For the load calculation module of the aquaculture cage, the effect of the cage on the fluid is incorporated by adding the net cage load to the source term of the computational equation. In this study, the net cage load is calculated using the Darcy-Forchheimer model, as illustrated in the following equation.

$$S_i = -\left(\sum_{j=1}^{3} D_{ij}\mu u_{rel,j} + \sum_{j=1}^{3} C_{ij}\frac{1}{2}\rho|u_{rel,j}|u_{rel,j}\right) \tag{20}$$

$$D = \begin{bmatrix} D_n & 0 & 0 \\ 0 & D_t & 0 \\ 0 & 0 & D_t \end{bmatrix}, C = \begin{bmatrix} C_n & 0 & 0 \\ 0 & C_t & 0 \\ 0 & 0 & C_t \end{bmatrix} \tag{21}$$

where S_i is the source term in the momentum equation, D_{ij} and C_{ij} represent the viscous and inertial terms, respectively, μ is the dynamic viscosity, ρ is the fluid density, and *n* and *t* denote the normal and tangential directions, respectively. u_{rel} represents the relative velocity considering the motion of the net cage. The implementation process of the equations is shown in Algorithm 1.

The motion of the net cage encompasses both translational and rotational movements. For each grid point in the net cage region, the relative velocity due to translational motion is uniform, while the relative velocity due to rotational motion is calculated based on the grid point's position relative to the rotation center. The formula is as follows:

$$\mathbf{U}_{\mathbf{rel}}^{\mathbf{r}} = \boldsymbol{\omega} \times \mathbf{r} \tag{22}$$

where $\mathbf{U}_{\mathbf{rel}}^{\mathbf{r}}$ represents the relative velocity of a grid cell due to rotational motion. $\boldsymbol{\omega}$ is the angular velocity vector, $\mathbf{r}$ is the rotational radius vector. The implementation process of Eq. (22) is in lines 5 to 10 of Algorithm 1. As the net cage moves continuously,

the Darcy-Forchheimer coefficient matrices (D, C) change within the global coordinate system. Consequently, it is essential to update these coefficients according to the net cage's specific position. Utilizing the six degrees of freedom motion information, the transformation matrix R. The updated coefficient matrix is:

$$\begin{cases} D'_{ij} = R_{ip} D_{pq} R_{jq} \\ C'_{ij} = R_{ip} D_{pq} R_{jq} \end{cases} \tag{23}$$

which corresponds to lines 2 and 3 of Algorithm 1. The lift and drag forces on the cells of the net are calculated using the following equations:

$$\begin{cases} F_d = \left(D_n \mu u_{rel} + \frac{1}{2} C_n \rho |u_{rel}| u_{rel} \right) V \\ F_l = \left(D_l \mu u_{rel} + \frac{1}{2} C_l \rho |u_{rel}| u_{rel} \right) V \end{cases} \tag{24}$$

where V is the cell volume on the net.

Algorithm 1: Coupled FOWT-cage calculation

Input: The Darcy-Forchheimer coefficient tensor *D* and *F*, the orientation tensor of the floating platform *orientation*, the angular velocity vector of floating platform *omega*, rotation center of floating platform *rotCenter*, the translation velocity of floating platform *velocity*, the scalarField of cells volume *V*, the scalarField of the fluid density ρ, the scalarField of dynamic viscosity μ, the vectorField of fluid velocity *U*.

Output: The cage loads vectors *force* and *moment*, the cage loads application point *refPoint*.

1. **forAll** *nets*[*i*] **do**
2. *D*[*i*] ← *orientation* * *D* * *orientation*^{T}
3. *F*[*i*] ← *orientation* * *F* * *orientation*^{T}
4. **forAll** *cells*[*j*] **do**
5. *omegaNorm* ← |*omega*|
6. *omegaAxis* ← *omega*/*omegaNorm*
7. *n* ← *omegaAxis*/|*omegaAxis*|
8. *projection* ← *rotCenter* + *n* * ((*cellCenter*[*j*] - *rotCenter*) * *n*)
9. *radius* ← *cellCentres*[*j*] – *projection*
10. *rotVelocity* ← *omegaNorm* * *n* ^ *radius*
11. *motionVelocity* ← *velocity* + *rotVelocity*
12. *forceDF*[*j*] ← *V*[*j*] * (*D*[*i*] * μ[*j*] * |*U*[*j*] - *motionVelocity*| + *F*[*i*] * 1/2 * ρ[*j*] * |*U*[*j*]| * *U*[*j*])
13. *momentDF*[*j*] ← (*cellCenter*[*j*] - *rotCenter*) ^ *forceDF*[*j*]

```
        force[i] += forceDF[j]
        moment[i] += momentDF[j]
        refPoint ←rotCenter
    end
end
```

Upon completing the net cage load calculation, a supplementary module was developed to store the net cage load. This module subsequently applies the load as an external force within the floating body's motion equations. In this study, the "darcyForchheimerCage" class was created in OpenFOAM. The net cage load, moment, and application point, calculated in this section, are stored within the "darcyForchheimerCage" class. During the computations, the net restraints are defined in the relevant files, facilitating the coupling between the net cage load calculation and the six-DoF motions of the platform.

3.4 Coupled wave-current loading module

Based on the second-order Stokes wave theory, this study considers the effect of uniform current in the same direction with the waves and incorporates the Doppler effect caused by the current velocity on the wave period. The flow function is integrated into the second-order Stokes wave theory, resulting in the following velocity potential function and wave surface function.

$$\phi = u_{current}x + \frac{\pi H}{kT}\frac{\cosh k(z+h)}{\sinh kh}\sin\theta' + \frac{3}{8}\frac{\pi^2 H}{kT}\left(\frac{H}{L}\right)\frac{\cosh 2k(z+h)}{\sinh^4 kh}\sin 2\theta' \quad (25)$$

$$\eta = \frac{H}{2}\left[cos\,\theta' + \frac{Hk}{8}\frac{\cosh(kh)\cdot(\cosh(2kh)+2)}{\sinh^3 kh}\cos 2\theta'\right] \quad (26)$$

$$\theta' = kx - \omega' t \quad (27)$$

In the equation, $\omega' = \frac{2\pi}{T} + ku_{current}$ represents the wave angular frequency

considering the effect of uniform current, where $u_{current}$ is the velocity of the current. In this study, the wave-current combined conditions are simulated using the wave-current coupling module developed in this research. The horizontal and vertical components of fluid velocity distribution are represented in the equations below.

$$u = u_{current} + \frac{H}{2}\omega\left[\frac{\cosh k(z+h)}{\sinh kh}\cos\theta + \frac{3}{8}Hk\frac{\cosh 2k(z+h)}{\sinh^4 kh}\cos 2\theta\right] \quad (28)$$

$$v = \frac{H}{2}\omega\left[\frac{\sinh k(z+h)}{\sinh kh}\sin\theta + \frac{3}{8}Hk\frac{\sinh 2k(z+h)}{\sinh^4 kh}\sin 2\theta\right] \quad (29)$$

The above equations are incorporated in the wave2Foam to further develop the wave-current coupling module.

4. Reliability validation of HybridMarineFoam solver

4.1 Validation of aquaculture cage module

4.1.1 Verification of mesh size of a cage net

To verify the impact of thickness of the porous media region on load calculation results, a simple computational model of the ultra-high molecular weight polyethylene (UHMWPE) aquaculture net cage was established (Hu et al., 2023; Zhao et al., 2024). The computational domain and mesh are depicted in Fig. 7. The inlet boundary was specified as a velocity inlet with an applied velocity of 1.2 m/s, while the outlet was defined as a zeroGradient boundary. All other boundaries were set to symmetric boundary conditions. The study examined the load calculations for porous media region thicknesses ranging from 0.05 m to 5 m, with each thickness represented by five grid cells. The Darcy-Forchheimer coefficients and load calculation results corresponding to various grid thicknesses are provided in Table 1. The findings indicate that the

thickness of the porous media region has minimal impact on the calculated net load.

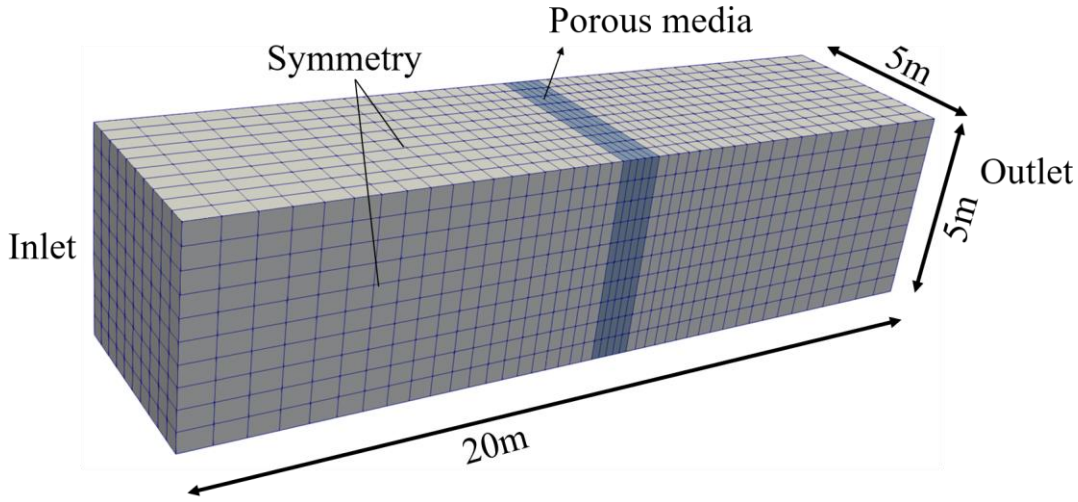

Fig. 7. Computation domain for the validation case.

Table. 1. Darcy-Forchheimer coefficients for each thickness of porous media region.

Thickness of porous media (m)	$D_n(\mathrm{m}^{-2})$	$D_t(\mathrm{m}^{-2})$	$C_n(\mathrm{m}^{-1})$	$C_t(\mathrm{m}^{-1})$	Force (kN)
0.2	1.75×10^5	1.47×10^5	3.0	0.42	11.75
0.5	7.00×10^5	5.89×10^5	1.20	0.17	11.75
1.0	3.50×10^5	2.94×10^5	0.60	0.084	11.74
2.0	1.75×10^4	1.47×10^4	0.30	0.042	11.73
4.0	8.75×10^3	7.36×10^3	0.15	0.021	11.72

To minimize the influence of grid size of the porous media on load calculation results, this study utilized a 2m thick porous media layer and performed a verification analysis on the effect of different grid sizes within the region. Grid sizes within the porous media region ranged from 0.2 m to 2 m, and the calculation results are presented in Table 2. The findings indicate that the grid size within the porous media region has negligible impact on the calculation results. In the simulation of the wind turbine with an integrated net cage structure, the computational domain is extensive, which significantly increases the modeling difficulty. Selecting an appropriate grid size that maintains calculation accuracy helps reduce modeling complexity and enhances

computational efficiency. For this study, a porous media region thickness of 2 m and a grid size of 0.5 m within the porous media region were chosen to model the aquaculture cage in the integrated structure.

Table. 2. Loads on porous media region in different mesh sizes.

Mesh size of porous media (m)	Force (kN)
0.2	11.81
0.5	11.73
1.0	11.44
2.0	10.85

4.1.2 Validation of the aquaculture cage motion module

In the aquaculture cage-floating platform coupling module developed for this study, relative velocity (Wang et al., 2022) plays a critical role in determining the net cage load. To assess whether the calculated aquaculture cage loads remain consistent under various relative velocity patterns, a simplified computational model was constructed. Referring to the model illustrated in Fig. 7, two conditions were analyzed. In condition 1, the flow velocity U_{in} was maintained at a certain value while the aquaculture cage underwent sinusoidal motion, as described below:

$$U_{motion} = A\sin(\omega t) \tag{30}$$

In Condition 2, the net cage is stationary, and the flow velocity varies according to the following equation:

$$U_{in} = U_0 - A\sin(\omega t) \tag{31}$$

This approach ensures that the relative velocities in both Conditions 1 and 2 are equivalent. In this study, the variations in net cage loads were analyzed using Equations (30) and (31) under the conditions U_0 = 1.2 m/s, A = 1 m, ω = 1.236 rad/s and U_0 =

2 m/s, A = 1 m, ω = 1.236 rad/s. Fig. 8 illustrates the variations in the calculated loads on the aquaculture cage for all conditions. The results demonstrate that, regardless of whether the change in relative velocity arises from the movement of the aquaculture cage or variations in flow velocity, the calculated loads remain consistent when the relative velocities are identical. This confirms the accuracy and reliability of the coupling module between the net cage and the floating platform.

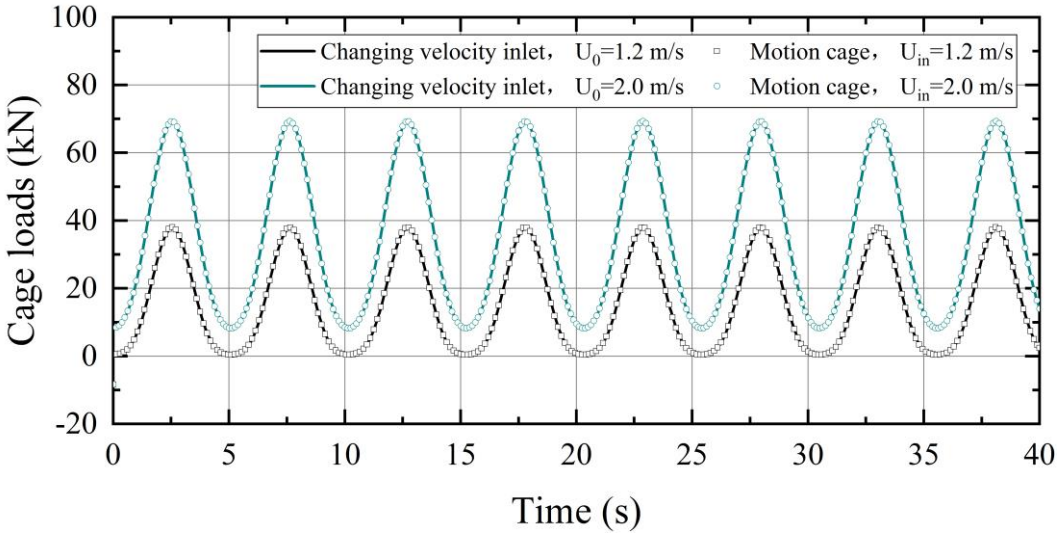

Fig. 8. Cage loads under moving cage and variable inlet velocity.

4.2 Validation of higher efficiency and accuracy of HybridMarineFoam solver

4.2.1 Validation of free decay test

This section uses the OC4 semi-submersible NREL 5MW wind turbine to validate the efficiency and accuracy of the developed HybridMarineFoam solver, where the multi-region coupled analysis module in this solver was also validated in our previous research (Cai et al., 2024). The model description for the OC4 semi-submersible NREL 5MW wind turbine are provided in Appendix A. In this study, free decay tests were conducted on surge, heave, and pitch motions using the HybridMarineFoam solver, obtaining the natural periods of the OC4 floating platform. As described in other studies,

the free decay tests of surge, heave and pitch DoFs were conducted with initial displacements of 22m, -3m and 8°, respectively. Notably, to align with simulations in the studies (Cheng et al., 2019; Tran and Kim, 2015), an additional surge stiffness of 7.39 kN/m is considered in this study, provided by the cable transferring data between the floating platform model and the computer during the experiment. Simulation data on natural periods were compared with experimental and other simulation results, detailed in Table 3, revealing close agreement. Specific results from the free decay tests of surge, heave, and pitch motions were compared with other CFD results, illustrated in Fig. 9. The surge free decay results from this study align with those reported by Tran and Kim (2015). Similarly, the heave free decay results closely correspond with findings by Liu et al. (2017). However, slight discrepancies were noted in the pitch motion free decay results compared to studies by Tran and Kim (2015) and Cheng et al. (2019). Overall, the CFD model of the floating platform in this study meets the computational requirements.

Table 3. Comparison of natural periods of the OC4 platform (Unit: s).

DoF	Exp (Coulling et al., 2013)	CFD (Tran and Kim, 2015)	CFD (Liu et al., 2017)	CFD (Cheng et al., 2019)	Present
Surge	107	108.1	107.2	108.3	111.7
Heave	17.5	17.8	17.5	17.58	17.9
Pitch	26.8	25.2	27.4	25.8	26.8

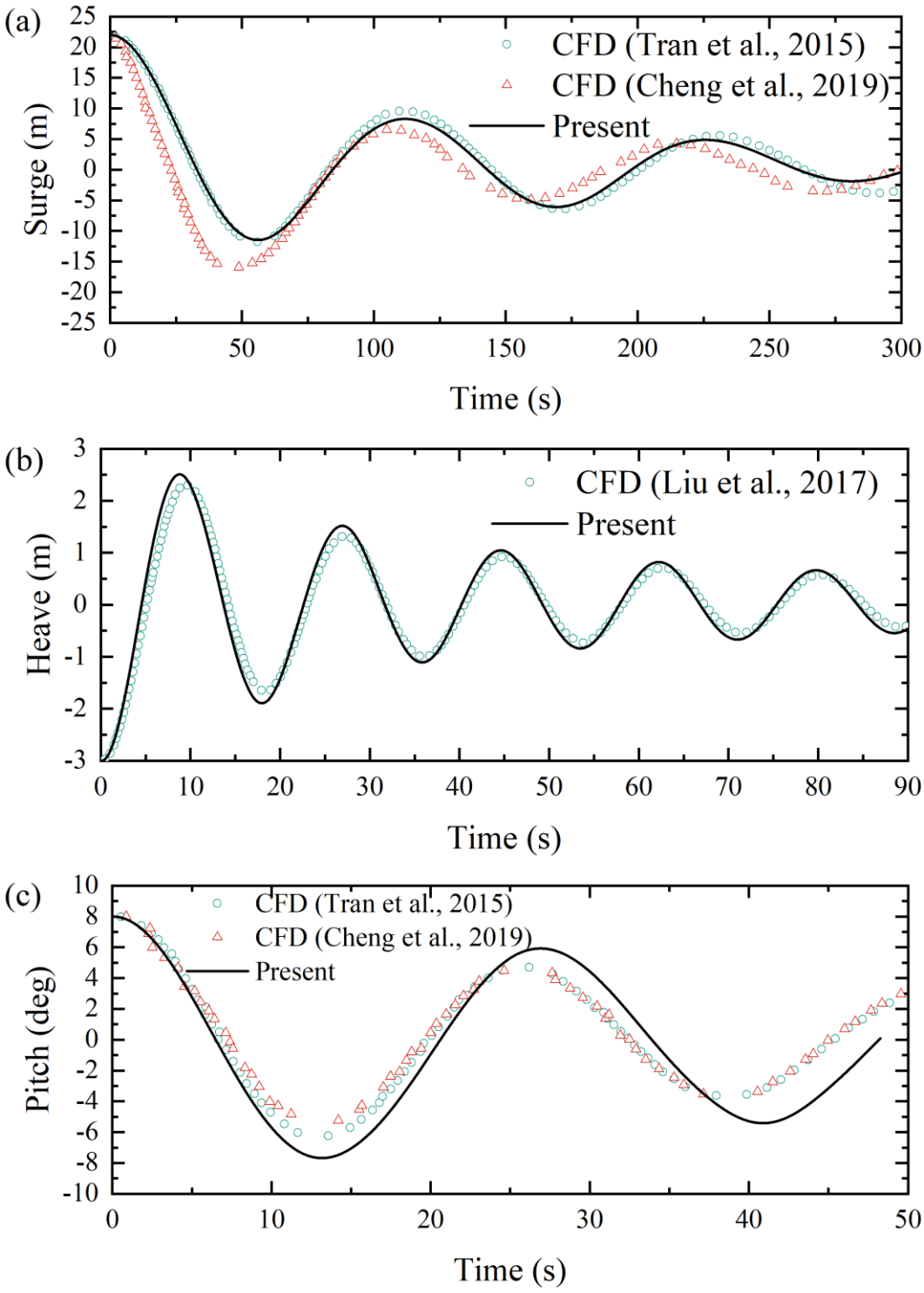

Fig. 9. Dynamic response of free decay test: (a) Surge free decay with 22 m initial displacement; (b) Heave free decay with -3 m displacement; (c) Pitch free decay with 8° initial rotation.

4.2.2 Validation of the dynamic response of NREL 5MW wind turbine

The study examines the unsteady aerodynamic characteristics, platform motion response, and mooring line behavior of a NREL 5MW FOWT under conditions of

regular waves and uniform wind. The wind speed is set as 11.4 m/s, and a regular wave with the wave period and height being 12.1 s and 7.58 m, respectively, is adopted herein for the case of 200 m water depth, where its wave steepness is calculated as 0.0332. The comparison of thrust, surge, heave, and pitch motions of the NREL 5MW FOWT system simulated by HybridMarineFoam solver and fully coupled method (Pericàs, 2022), along with results from other researchers, is illustrated in Figs. 10 and 11. Overall, the figures demonstrates good agreements among the simulation results. Motion response amplitudes calculated by the HybridMarineFoam solver are slightly larger and exhibit closer alignment with the findings of Tran and Kim (2016). It is important to note that some differences exist between the CFD-based results and those obtained from FAST, particularly in the heave and pitch responses. These differences can be attributed to the fundamental distinctions between the two methods: FAST relies on a simplified potential flow theory, while the CFD approach solves the full N-S equations. The N-S-based model provides a more detailed representation of viscous effects and turbulence, which are not fully captured by FAST's potential flow approach, leading to lower predicted amplitudes in the CFD simulations.

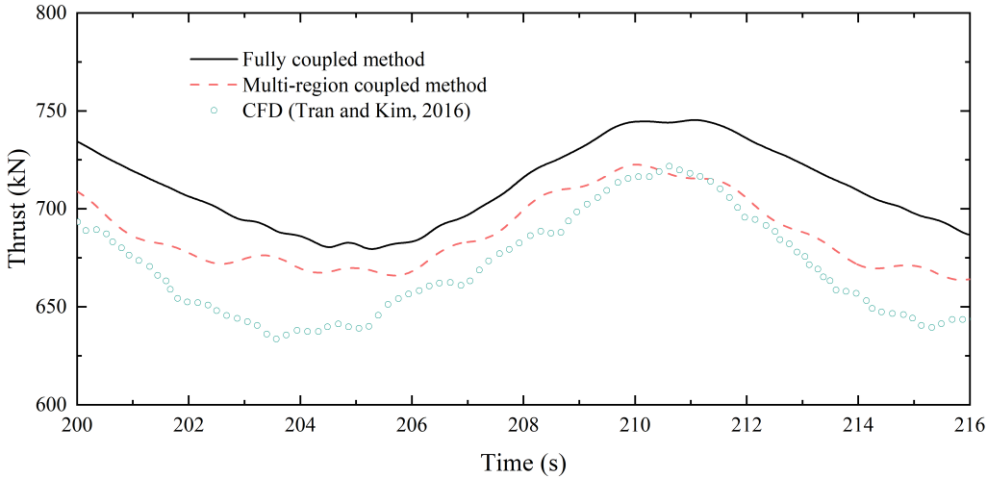

Fig. 10. Aerodynamic thrust of 5MW FOWT under combined wave and wind.

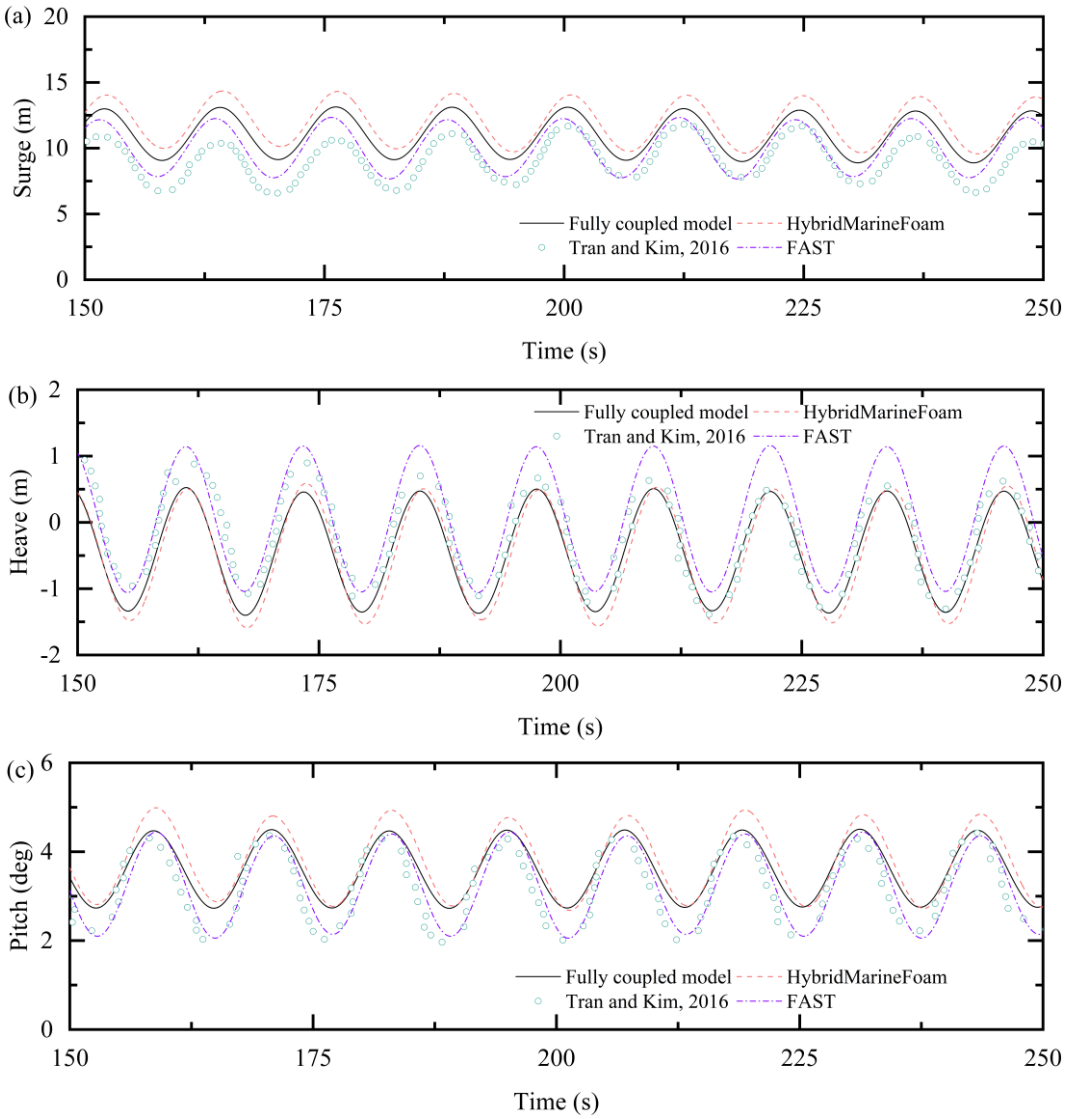

Fig. 11. Motion responses of 5MW FOWT under combined wave and wind: (a) Surge, (b) Heave and (c) Pitch.

The comparison of simulated mooring line tensions is presented in Fig. 12, with the average tension values listed in Table 4. The fluctuation amplitude of the tension in mooring line #1, calculated using both the fully coupled method and the HybridMarineFoam solver, is significantly larger than the fluctuation observed in the static mooring line tension reported by Tran and Kim (2016). It is also noted that the CFD results given by Tran and Kim (2016) indicate a higher average tension for

mooring line #1, whereas their FAST-calculated average tension aligns more closely with the values obtained by the HybridMarineFoam solver. In contrast, the average tension for mooring line #2, as calculated by the HybridMarineFoam solver, is lower than the values reported by Tran and Kim (2016). This discrepancy can be attributed to differences in the modeling approaches. Tran and Kim (2016) adopted a static catenary method for mooring line modeling, while our study employs a dynamic lumped-mass method, which can incorporate dynamic effects of platform motions and wave interactions more properly.

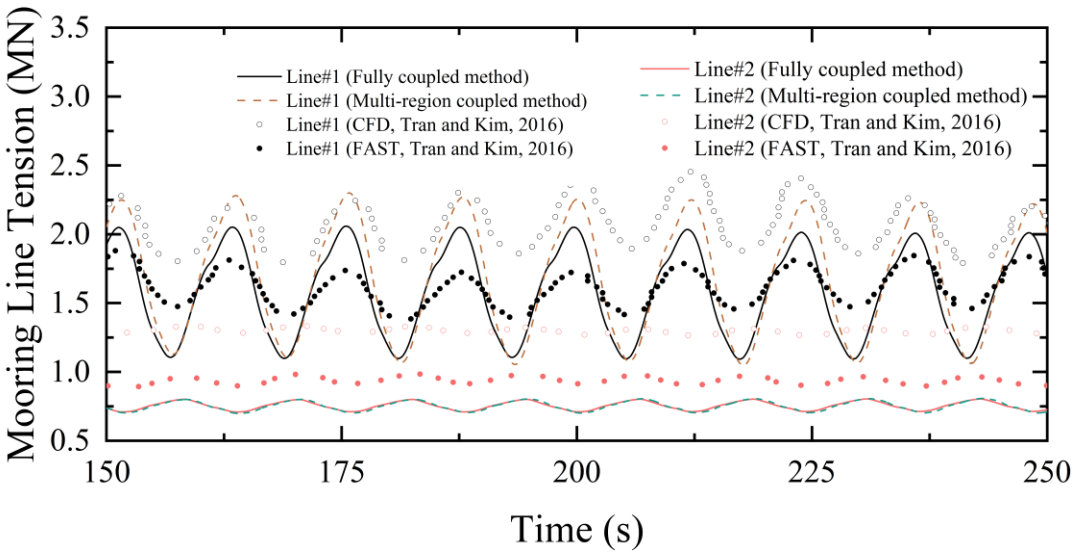

Fig. 12. Mooring line tension for lines #1 and #2 of NREL 5MW FOWT under combined regular wave and sheared wind.

Table 4. Average value of Line#1 and Line#2 with different methods.

Average value	Line#1 (MN)	Line#2 (MN)
Fully coupled method	1.585	0.755
Multi-region coupled method	1.691	0.754
CFD, Tran and Kim, 2016	2.086	1.299
FAST, Tran and Kim, 2016	1.616	0.939

4.2.3 Comparison of computational efficiency

In order to compare the computational efficiency between the fully coupled method

and HybridMarineFoam solver, identical iterative and solver settings are employed in this study. The simulations utilize a time step of 0.01s and are conducted on a 96-core high-performance computing system with AMD Epyc 7642 CPU. At each time step, two outer corrector loops and two pressure correction loops are executed. To ensure convergence, the residual for each iteration is set to 1e-8. The number of grid cells and computation time per time step for different models and methods are shown in Table 5. It is evident that the HybridMarineFoam solver proposed in this study reduces the number of grid cells and significantly enhances computational efficiency. Under identical conditions, 400s-simulation now requires only 78 hours to compute for NREL 5MW FOWT, effectively nearly doubling the computational efficiency relative to the fully coupled approach.

Table 5. Analysis of simulation efficiency for different method.

Model	Method	Cell Number (in million)	Simulation time (h)
NREL 5MW	Fully coupled	2.78	133
	Multi-region coupled	2.01	78

5. Application of HybridMarineFoam solver on integrated structure

5.1 Description of the integrated structure

In this study, the VolturnUS-S semi-submersible IEA 15 MW FOWT serves as the core structural component of the integrated system, detailed structural parameters are provided in Appendix B. The aquaculture cage consists of four net panels encircling the floating platform, forming an enclosed space together with the platform. As depicted in Fig. 13(a), three of the net panels wrap around the platform, and the bottom plane net is illustrated in Fig. 13(b). The integration of the VolturnUS-S semi-submersible IEA

15 MW wind turbine with these plane nets, as shown in Fig. 14, results in a combined FOWT and aquaculture cage system. The characteristics of this integrated structure is set to match those specified for the 15 MW FOWT, enabling an assessment of how the aquaculture cage affects the performance of the FOWT.

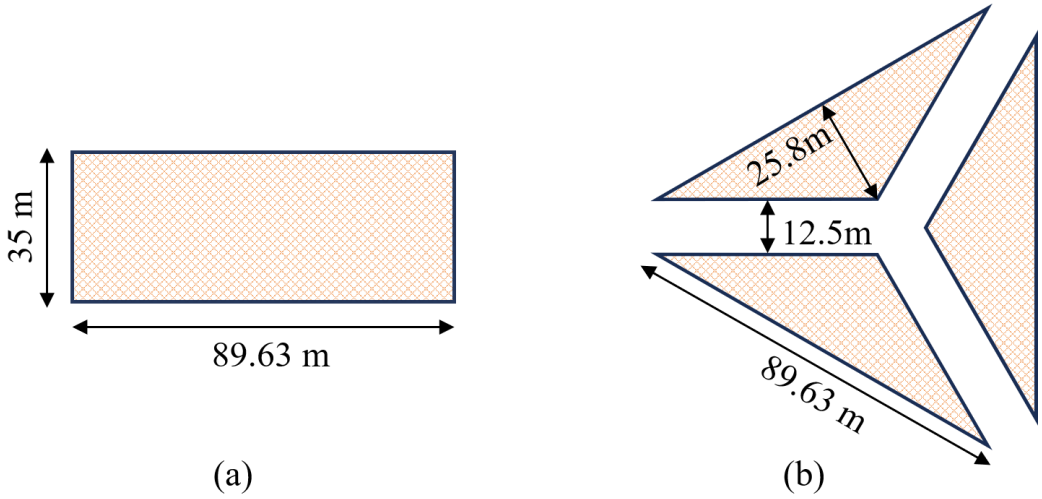

Fig. 13. Side (a) and bottom (b) plane net of the aquaculture cage.

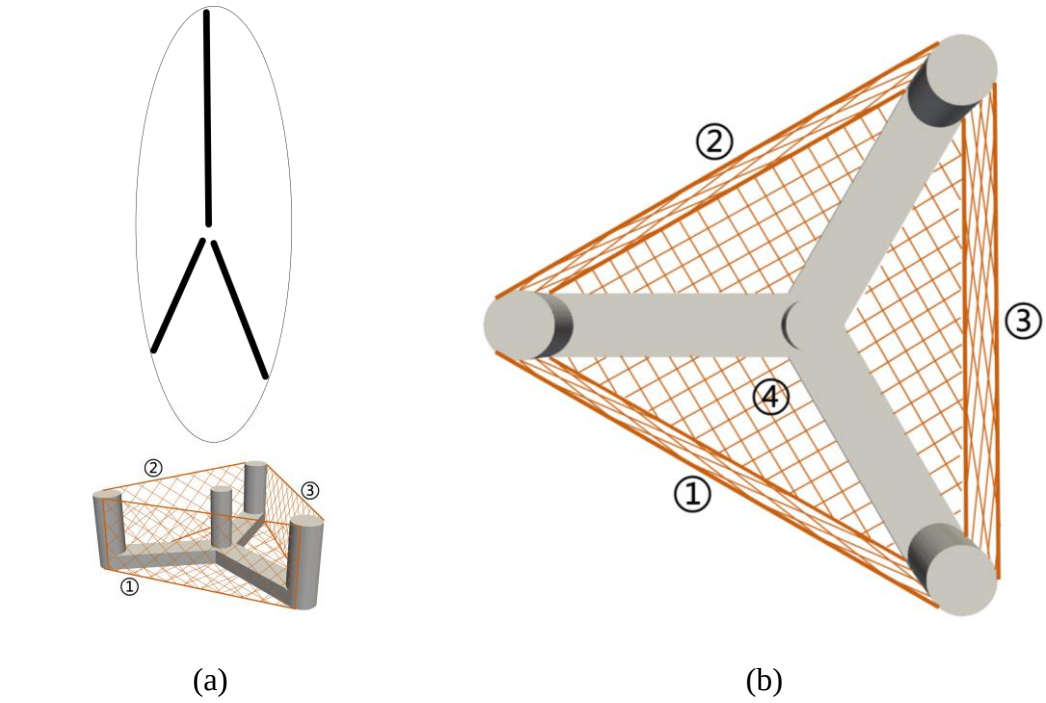

Fig. 14. Schematic of the integrated structure of IEA 15MW wind turbine and aquaculture cage.

In the simulation of the integrated FOWT and aquaculture cage system with HybridMarineFoam, the computational domain is divided into two separate regions. The floating platform's computational domain measures 1300 m × 500 m × 400 m, as depicted in Fig. 15, while the wind turbine rotor domain spans 900 m × 600 m × 400 m, illustrated in Fig. 16. The distance between the floating platform and the inlet boundary is 550 m. At the inlet boundary, a 350 m section is designated as the wave generation zone, whereas the 450 m segment serves as the wave absorption zone at the outlet boundary. The detailed simulation mesh is shown in Figs. 17 and 18. A total of 2.77 million grid cells were generated using snappyHexMesh in OpenFOAM, with refined mesh regions near the free surface and around the platform. The floating platform domain contains 1.82 million grid cells, and the rotor domain contains 0.95 million grid cells. To ensure wave generation accuracy while optimizing the grid count, the mesh size is uniform from the inlet boundary to the platform and gradually increases from the platform towards the outlet boundary. At the free surface, grid element sizes are 4 m in the X-direction and 1 m in the Z-direction. Near the platform, the mesh sizes vary from a maximum of 2 m to a minimum of 0.25 m. Five layers of boundary cells are extruded from the platform surface, with a growth ratio of 1.2, starting at a height of 0.012 m for the first cell away from the surface. In the aquaculture cage region, the mesh is refined to 0.5 m, and in the wind turbine rotor region, the mesh size is refined to 1 m to ensure precise computation of wind turbine loads.

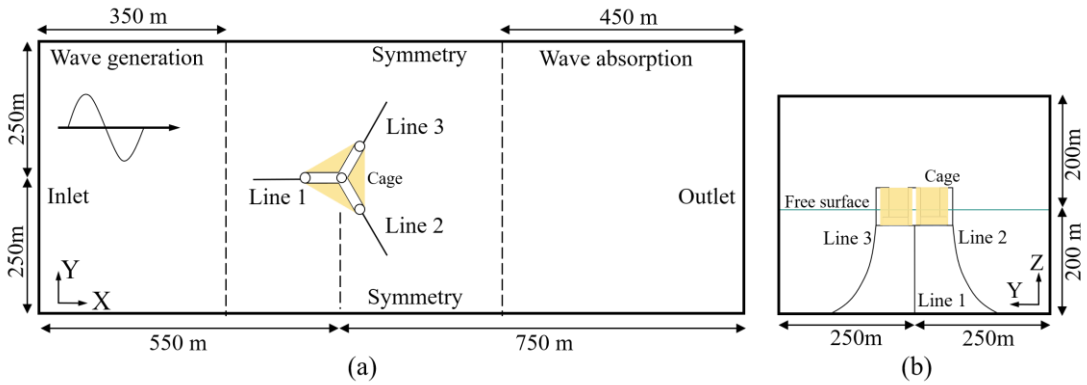

Fig. 15. Floating platform region of HybridMarineFoam solver for the integrated structure. (a) Top view; (b) Inlet view.

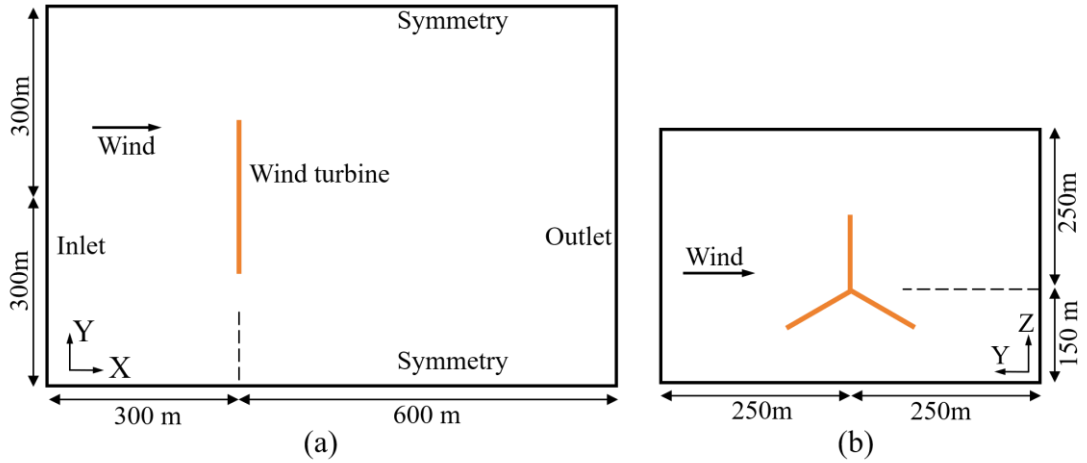

Fig. 16. Wind turbine region of HybridMarineFoam solver for IEA 15MW wind turbine rotor. (a) Top view; (b) Inlet view.

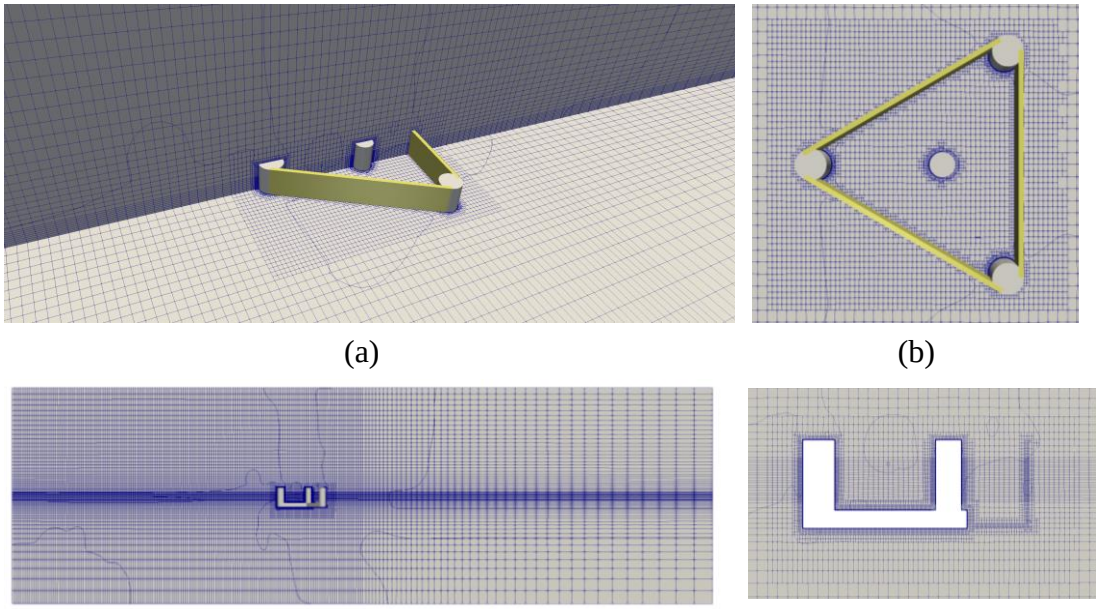

Fig. 17. Computational mesh of the floating platform region: (a) Overview, (b) Top view, (c) Side view, (d) Detailed mesh near the platform. (The yellow area

represents the porous media region of the aquaculture net cage.)

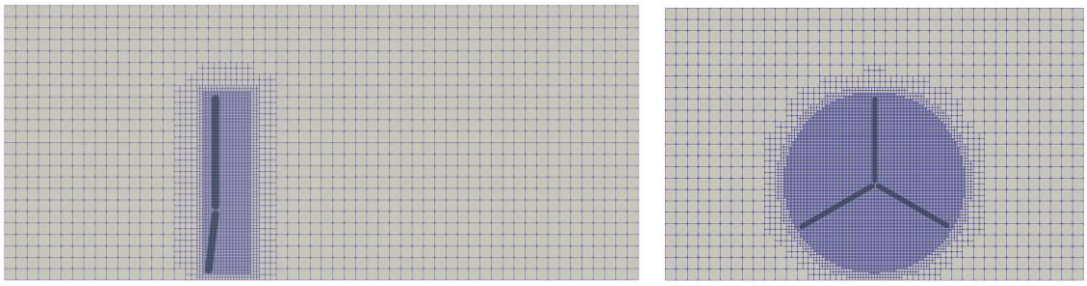

(a) (b)

Fig. 18. Computational mesh of the wind turbine rotor region: (a) Side view, (b) Front view.

5.2 Validation of the IEA 15 MW wind turbine

5.2.1 Validation of thrust of the wind turbine rotor

The rotor domain (Fig. 16) within the HybridMarineFoam framework is utilized for validating thrust measurements. Fig. 19 displays the aerodynamic thrust values calculated for the 15 MW wind turbine across various grid resolutions, with the medium mesh configuration identical to that shown in Fig. 18. Table 6 summarizes the average thrust values recorded from 75 to 100 s and provides a detailed analysis of the variations in aerodynamic thrust associated with different grid sizes. The results indicate minimal differences in thrust values among the three grid sizes, with the variation between the medium and fine grids being less than 1%. This observation confirms that the medium grid resolution meets the required accuracy standards. Therefore, the medium grid size will be used for refining the rotor domain in future coupled simulations.

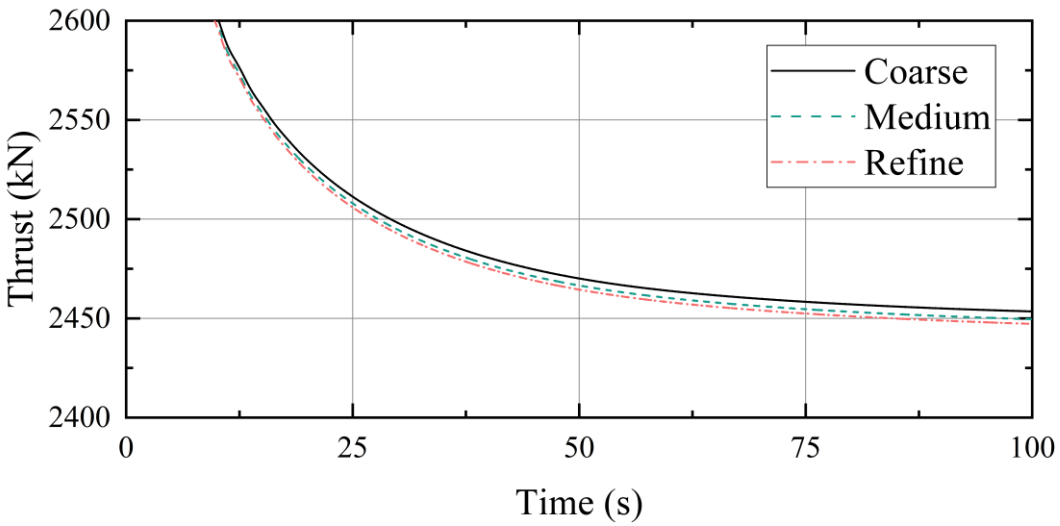

Fig. 19. Mesh convergence analysis of thrust of IEA 15 MW wind turbine.

Table 6. Analysis of grid convergence of thrust.

Mesh	Cell Number (in million)	Thrust (kN)
Coarse	0.64	2.462 (0.85%)
Medium	0.95	2.450 (0.37%)
Refine	1.42	2.441 (0%)

5.2.2 Validation of hydrodynamic characteristics of VolturnUS-S semi-submersible platform

In this study, free decay tests were conducted to determine the natural periods of the VolturnUS-S semi-submersible platform, focusing on surge, heave, and pitch motions using the floating platform domain (see Figs. 15 and 17). The tests involved initial displacements of 30 m for surge, 5 m for heave, and 10° for pitch. The simulation data for natural frequencies were compared with results from previous report (Allen, 2020), as detailed in Table 7, showing close agreement. To validate the accuracy of the simulations, two cases of regular wave with the period and height being (12.1 s, 7.58 m) and (9.7 s, 3.66 m), respectively, were adopted, where the corresponding wave steepness are 0.0332 and 0.0249. The simulated response amplitude operator (RAO) results were compared with literature values, as presented in Table 8. Although the RAO

simulation results in this study are slightly lower than those in the literature, with a maximum deviation of approximately 5%, these differences can be attributed to the use of potential flow theory in previous studies (Allen, 2020) versus the CFD methods employed here. Nevertheless, the results indicate that the computational model used in this study for estimating the motion response of the floating structure is generally reliable.

Table 7. Comparison of natural frequency of the VolturnUS-S semi-submersible platform (units: Hz).

DoF	report	Present
Surge	0.007	0.007
Heave	0.049	0.046
Pitch	0.036	0.033

Table 8. RAO of the VolturnUS-S semi-submersible platform motion responses.

	RAO (Wave height = 7.58 m, period = 12.1 s)			RAO (Wave height = 3.66 m, period = 9.7 s)		
	Surge	Heave	Pitch	Surge	Heave	Pitch
Report (Allen, 2020)	0.512	0.512	0.212	0.299	0.331	0.269
Present	0.498	0.504	0.208	0.283	0.318	0.255

5.3 The motion responses of the integrated structure

This study investigates the dynamic response and flow field characteristics of a FOWT integrated with an aquaculture cage under the influence of wind, wave, and current loads. Additionally, it analyzes the impact of the net cage on the wind turbine's aerodynamic and hydrodynamic performance. To achieve this, eight computational cases were defined, covering a range of wind speeds, wave heights, and current velocities, as well as configurations with and without the net cage, as detailed in Table 9. The wind field was modeled as uniform, while the waves were represented as regular.

Ocean currents were simulated using a wave-current coupling module previously developed, which incorporates the Doppler effect in the wave-current interaction. Consequently, when ocean currents are present, the observed wave period is reduced compared to the set wave period.

Table. 9. Case settings.

Case	Wind speed (m/s)	Wave height (m)	Wave period (s)	wave steepness(-)	Current velocity (m/s)	Froude number(-)	Cage
#1	10.59	7.58	12.1	0.0332	-	-	Without cage
#2	10.59	7.58	12.1	0.0332	-	-	With cage
#3	7	3.66	9.7	0.0249	-	-	Without cage
#4	7	3.66	9.7	0.0249	-	-	With cage
#5	7	3.66	9.7	0.0249	0.5	0.0156	Without cage
#6	7	3.66	9.7	0.0249	0.5	0.0156	With cage
#7	7	3.66	9.7	0.0249	1	0.0313	Without cage
#8	7	3.66	9.7	0.0249	1	0.0313	With cage

Fig. 20 presents the surge, heave, and pitch motion responses, with the mean values and amplitudes detailed in Table 10. Overall, the integration of the net cage significantly impacts the mean surge position of the integrated structure. In the absence of ocean currents, the effect of the net cage on the mean surge position is particularly pronounced at lower wave height cases. Specifically, in cases 1 and 2, the mean surge position increases by 2.077 m when the net cage is present. In cases 3 and 4, which involve lower wave heights, this increase is more substantial, reaching 4.127 m. The presence of ocean currents further increases the mean surge position. As current speeds increase, the effect of the net cage becomes even more pronounced. At a current speed of 0.5 m/s, the mean surge position rises by 4.199 m with the net cage compared to its absence. At a current speed of 1 m/s, this increase is even more significant, amounting to 7.699 m. Moreover, the net cage also affects the surge motion amplitude. Without ocean currents,

the increase in surge amplitude is more pronounced at higher wave heights. However, at lower wave heights, the surge motion amplitude with the net cage shows only a marginal increase compared to when it is not present. Notably, at a current speed of 0.5 m/s, the surge motion amplitude with the net cage is slightly lower than without it, though the difference is minimal. At a current speed of 1 m/s, the surge motion amplitude increases significantly with the presence of the net cage.

The presence of the net cage exerts a minimal effect on heave motion. As indicated in Table 10, at higher wave heights, the heave motion remains largely unchanged regardless of the net cage's presence. Conversely, at lower wave heights, the net cage tends to lower the mean heave position, with this effect becoming more pronounced as current speeds increase. It is noteworthy that an increase in current speed consistently raises the mean heave position, irrespective of the net cage's presence. In contrast, the net cage generally decreases the amplitude of heave motion, particularly at lower wave heights. Fig. 20(c) illustrates that the net cage significantly reduces mean pitch motion while increasing pitch motion amplitude. Unlike surge and heave motions, the net cage more effectively decreases the mean pitch motion at higher wave heights compared to lower wave heights. Specifically, in cases 1 and 2, the mean pitch reduces by 0.261° with the net cage, whereas in cases 3 and 4, the reduction is only 0.10°. Furthermore, the effect of the net cage on reducing mean pitch motion becomes more evident as current speeds rise. At a current speed of 0.5 m/s, the mean pitch is 2.840° without the net cage and 2.622° with it. At a current speed of 1 m/s, the mean pitch is 2.777° without the net cage and 2.491° with it. Additionally, while pitch amplitude remains

relatively stable with changing current speeds in the absence of the net cage, it increases significantly with the net cage. Specifically, at current speeds of 0.5 m/s and 1 m/s, the pitch amplitudes are 0.775°, 0.833°, and 0.851°, respectively.

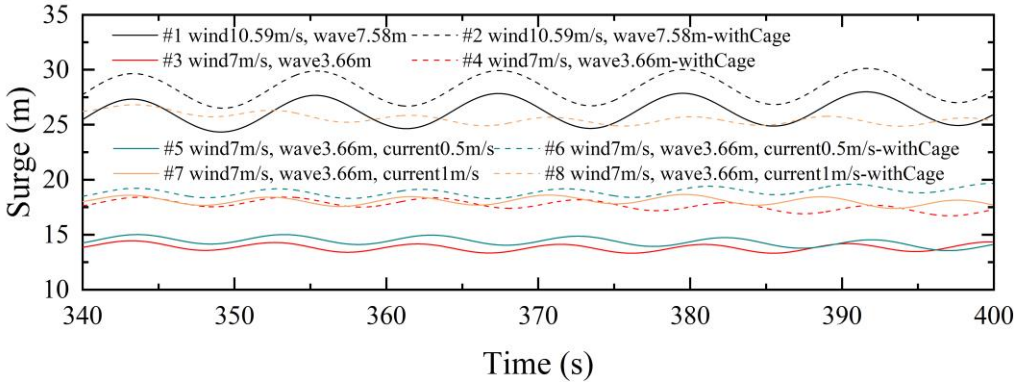

(a) Surge

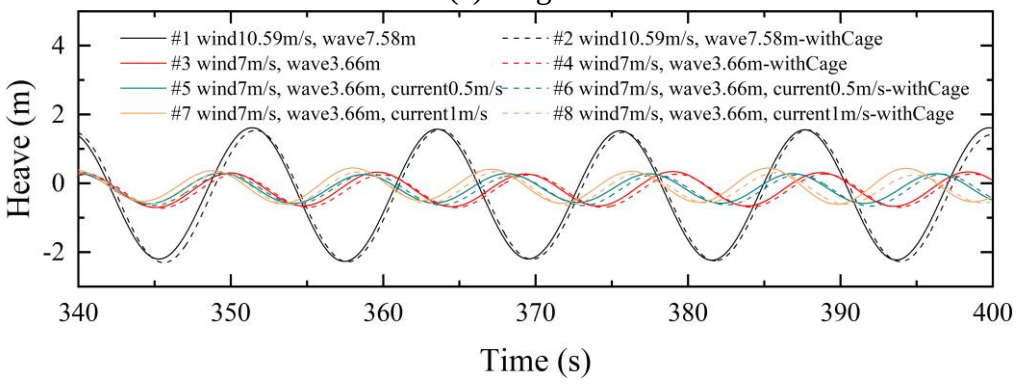

(b) Heave

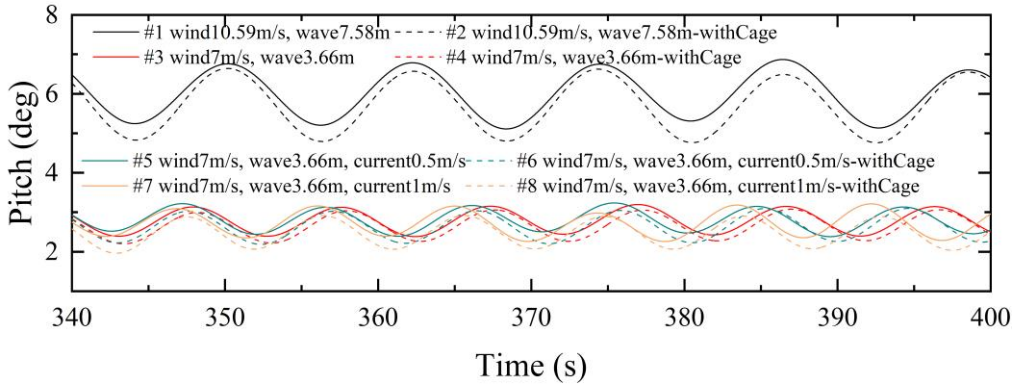

(c) Pitch

Fig. 20. Motion responses of integrated structure under different cases: (a) Surge, (b) Heave and (c) Pitch.

Table. 10. Mean values and amplitudes of the integrated structure motion responses

Case	Mean value (m, m, deg)			Amplitude (m, m, deg)		
	Surge	Heave	Pitch	Surge	Heave	Pitch

#1	26.253	-0.310	5.950	3.026	3.768	1.675
#2	28.330	-0.320	5.689	3.191	3.760	1.769
#3	13.752	-0.175	2.755	0.902	0.998	0.742
#4	17.879	-0.228	2.651	0.906	0.948	0.775
#5	14.510	-0.156	2.840	0.887	0.825	0.665
#6	18.709	-0.173	2.622	0.886	0.914	0.833
#7	18.079	-0.028	2.777	0.764	0.951	0.767
#8	25.778	-0.129	2.491	0.846	0.910	0.851

5.4 The hydrodynamic loads on the net cage and floating platform

The variations in loads on individual net panels and the entire net cage in the X and Z directions under different conditions are shown in Figs. 21 and 22. The numbering of each net panel is indicated in Fig. 14. Net panels 1, 2, and 3 surround the floating platform, with nets 1 and 2 symmetrically aligned along the X-axis, and net 4 positioned at the bottom of the floating platform. The load variations for nets1 and 2 are essentially identical, so only the results for net 1 are presented in this study. Overall, the load on the net panels in the X direction varies sinusoidally with wave propagation. When the wave height is greater, the load fluctuations on the net panels are also larger. Specifically, the X-direction load fluctuation amplitude is greatest for net 3 and smallest for net 4. The area of net 1 facing the waves is approximately half that of net 3, and correspondingly, the fluctuation amplitude of the X-direction load on net 1 is roughly half of that on net 3. Furthermore, at the same wave height, an increase in current speed results in an increased load on the net cage. As shown in Eq. (20), the load on the net cage is proportional to the square of the relative velocity. When the current speed increases from 0 to 0.5 m/s, the load on the net cage slightly increases. However, when the current speed further increases from 0.5 m/s to 1 m/s, the X-direction load on the net cage increases significantly. Additionally, the increase in current speed also

significantly amplifies the load fluctuation amplitude on the net cage, as indicated in Table 11. When the current speed increases from 0 to 0.5 m/s, the fluctuation amplitude of the X-direction load on each net slightly increases, whereas increasing the current speed from 0.5 m/s to 1 m/s leads to a significant rise in the fluctuation amplitude of the x-direction load on the net panels.

In Fig. 22, larger wave heights result in greater fluctuations in the Z-direction loads on the net panels, which is particularly evident for nets 1 and 4. For net 1, under case 2 with a wave height of 7.58 m, the fluctuation amplitude of the Z-direction load is approximately four times that of case 1 with a wave height of 3.66 m. For net 4, the amplitude is about five times greater compared to the other cases. The Z-direction load on net 3 also increases with wave height, though not as significantly as for the other nets. Conversely, the increase in current speed has a negligible effect on the fluctuation amplitude of the Z-direction load on the net panels. For the total Z-direction load on the net panels, the fluctuation amplitude is 149.54 kN without current, 158.58 kN at a current speed of 0.5 m/s, and 198.64 kN at a current speed of 1 m/s. Nevertheless, as the current speed increases, there is a slight increase in the Z-direction load on the net panels.

Notably, nets 1 and 4 tend to experience loads in the negative Z-direction, while the load on net 3 fluctuates in both the positive and negative Z-directions. According to Eq (20), the load on the net cage is primarily influenced by the relative velocity, which is affected by both the motion speed of the net panels and the fluid flow speed. As waves pass through, water particles in the waves undergo oscillatory motion in the Z-direction,

with the flow speed being largely symmetrical. In addition to the heave motion, pitch motion also induces movement of the net panels in the Z-direction. However, the vertical motion caused by pitch is difficult to quantify because nets 1, 2, and 4 are located on either side of the rotation center. Pitch motion causes one side of the net panels to move in the positive Z-direction and the other side in the negative Z-direction. Simultaneously, the complex movement of the net panels, combined with the flow speed as waves pass through, leads to intricate relative velocities at specific points on the net panels. This complexity might explain why nets 1 and 4 are more prone to negative Z-direction loads. In contrast, net 3 is entirely on one side of the rotation center, resulting in relatively less complex motion. Therefore, the load on net 3 tends to fluctuate in both the positive and negative Z-directions and follows a sinusoidal pattern. The Z-direction load variations on nets 1, 2, and 4 do not exhibit a clear pattern, but the changes are periodic, matching the wave cycles.

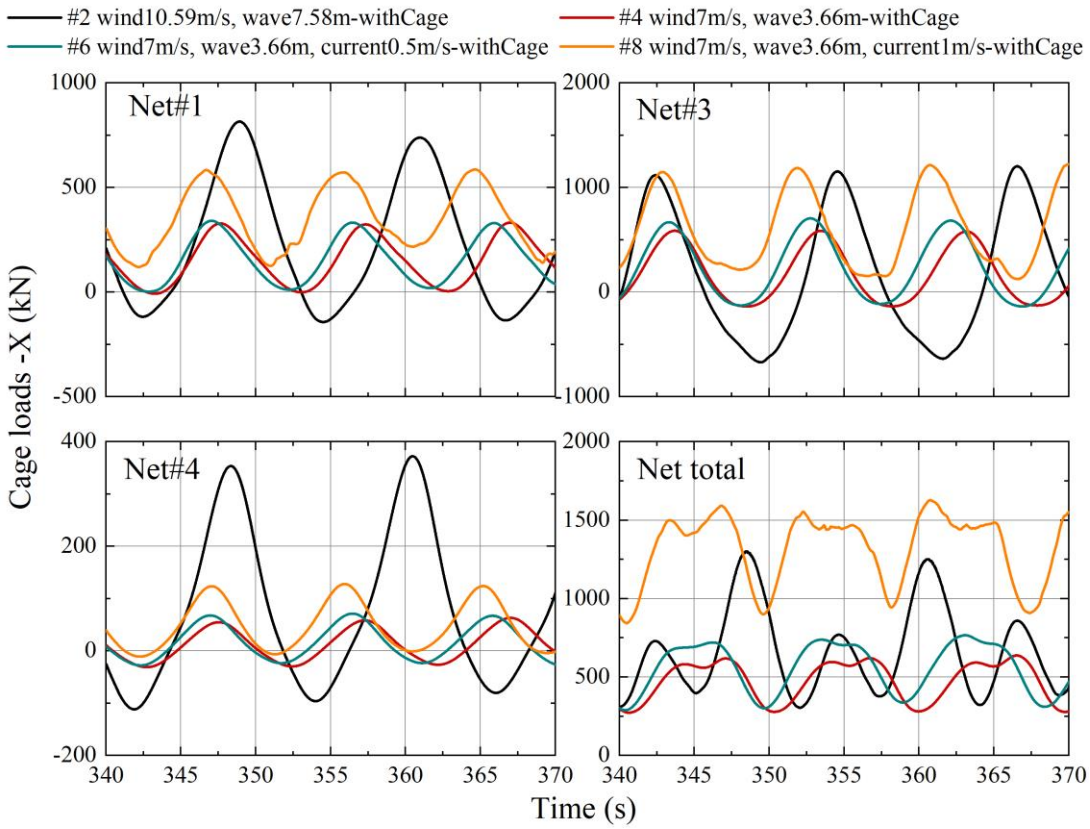

Fig. 21. The load of each net and total net cage in the X direction.

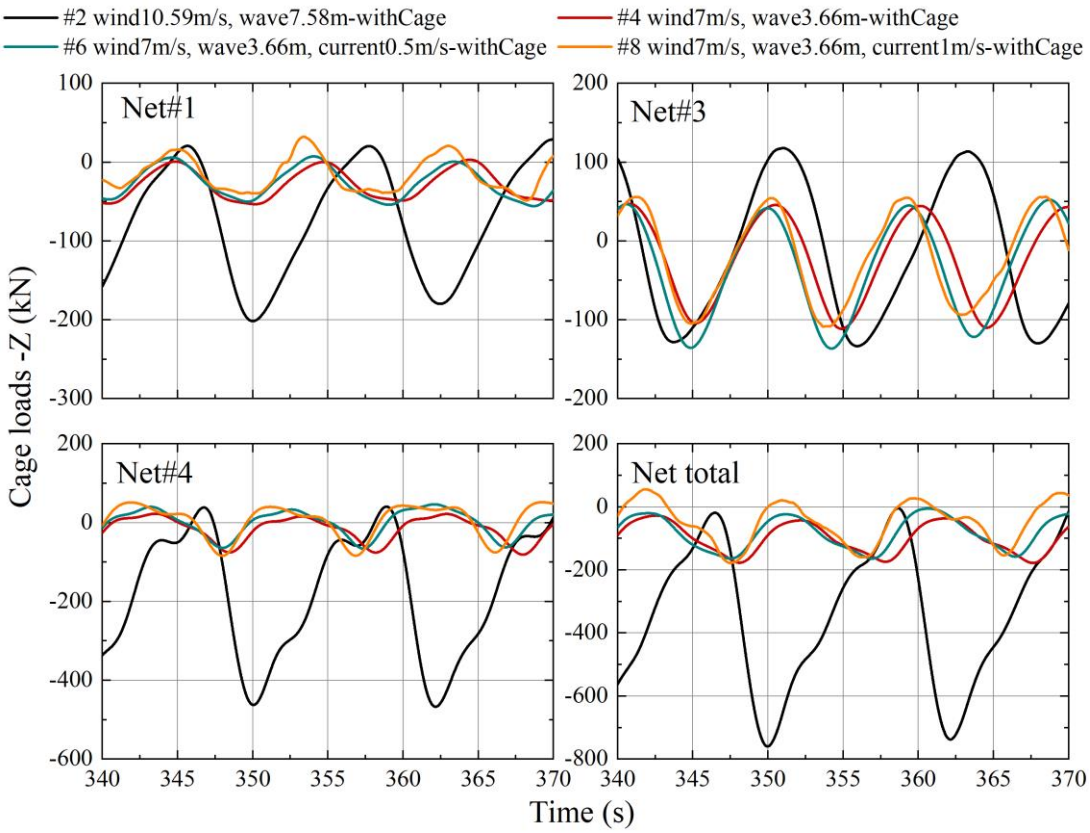

Fig. 22. The load of each net and total net cage in the Z direction.

Table. 11. Load amplitudes of net in x and z directions.

Case	Amplitude in X direction (kN)				Amplitude in Z direction (kN)			
	Net1	Net3	Net4	Net total	Net1	Net3	Net4	Net total
#2	957.89	1789.14	449.61	995.07	222.23	251.19	497.06	740.97
#4	329.33	720.79	84.51	340.28	54.04	156.96	98.28	149.54
#6	329.65	817.92	91.21	419.12	55.85	178.11	104.34	158.58
#8	458.03	1032.45	130.09	447.82	72.05	162.90	135.45	198.64

The X-direction loads on the platform and the net cage are depicted in Fig. 23. In cases including the net cage, the fluctuation amplitude of the total load on the platform and the net cage is marginally higher than the fluctuation amplitude of the platform load in cases without the net cage. Conversely, the fluctuation amplitude of the net cage load is significantly smaller than that of the platform load, being only 1/20 to 1/30 of the latter. This disparity can explain the slightly larger surge motion amplitude observed in cases with the net cage, as shown in Fig. 20(a). Additionally, in cases with the net cage, the fluctuation amplitude of the platform load alone exceeds that of the platform load in cases without the net cage. As the current speed increases, the fluctuation amplitudes of the loads on both the platform and the net cage also rise. The presence of the net cage contributes additional positive X-direction loads to the integrated structure, resulting in an increased average surge position.

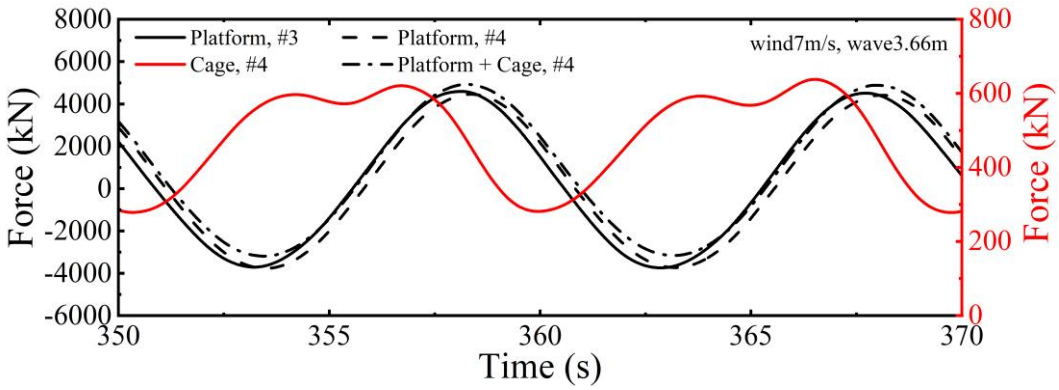

(a) Cases 3 and 4

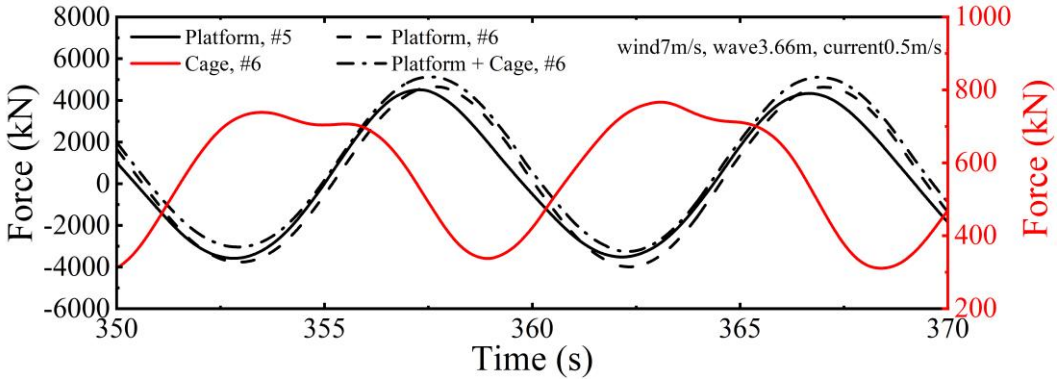

(b) Cases 5 and 6

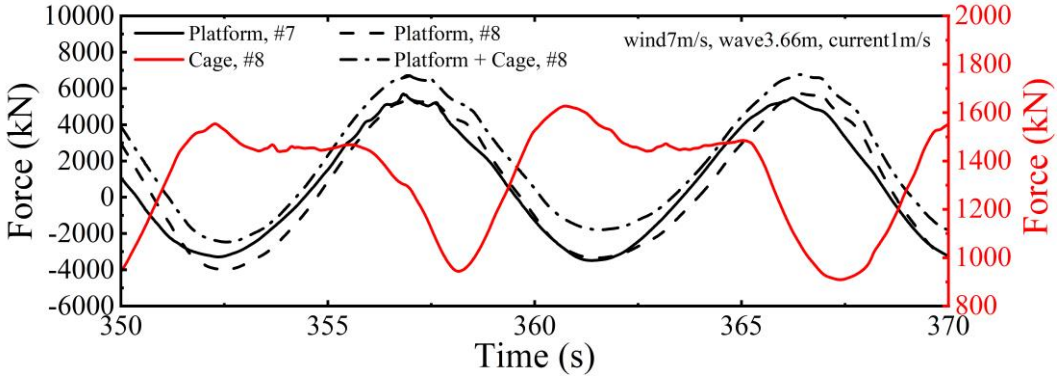

(c) Cases 7 and 8

Fig. 23. The load of platform and total net cage in the X direction: (a) Cases 3 and 4, (b) Cases 5 and 6, (c) Cases 7 and 8.

5.5 The aerodynamic loads on the rotor

The thrust of the rotor under different cases is shown in Fig. 24 and Table 12. Overall, the presence of the net cage significantly increases the amplitude of the rotor thrust. As shown in Fig. 20, both the presence of the net cage and the increase in current speed amplify the surge and pitch motions of the floating platform, resulting in greater fluctuations in the relative velocity of the rotor in the incoming flow direction, thereby increasing thrust fluctuations. In cases with higher wave heights (cases 1 and 2), the presence of the net cage leads to a larger increase in thrust amplitude, with an increase of 43.8 kN. In cases with lower wave heights (cases 3 and 4), the net cage presence only increases the thrust amplitude by 7.6 kN. On the other hand, as the current speed

increases, the thrust amplitude of the rotor also increases. Furthermore, with increasing current speed, the presence of the net cage makes the increase in thrust fluctuation amplitude more pronounced. When the current speed is 0.5 m/s, the presence of the net cage increases the thrust amplitude by 9.7 kN, while at a current speed of 1 m/s, the presence of the net cage increases the thrust fluctuation amplitude by 28.8 kN.

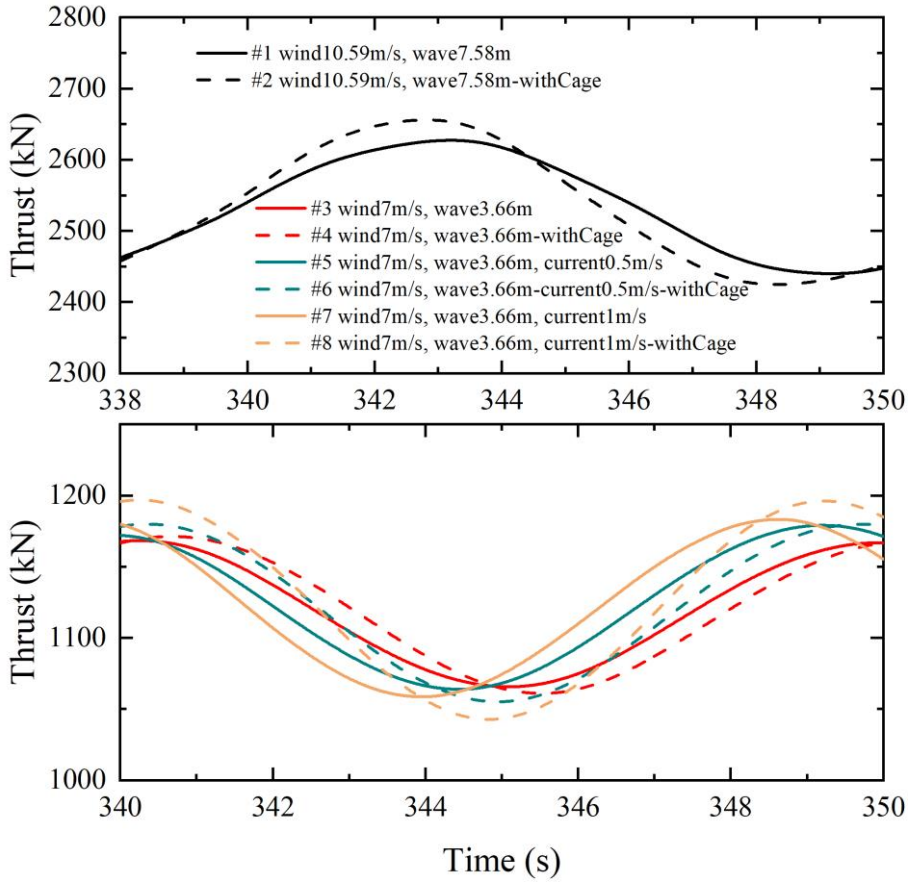

Fig. 24. Aerodynamic thrust of integrated structure under different cases.

Table. 12. Thrust amplitudes of different cases.

Case	Thrust amplitude (kN)
#1	187.3
#2	231.1
#3	102.6
#4	110.2
#5	115.1
#6	124.8
#7	124.5
#8	153.3

5.6 Flow field characteristics around the net cage

The wave field variations over one cycle for cases with and without the net cage, and the X-direction velocity variations at a section 10 m below the surface, are depicted in Figs. 25, 26, 27 and 28. Overall, the presence of the net cage has a negligible impact on the wave field. In the study by Bi et al. (2017), wave height attenuation after passing through a single net cage was found to be less than 1%. In this study, it is noteworthy that due to wave scattering, a higher wave peak appears after the first pontoon. When the net cage is present, the magnitude of this wave peak is significantly larger, as shown in Figs. 25(5d), (6d) and Figs. 26(7d), (8d). Additionally, this wave peak becomes more pronounced at higher flow speeds.

In Figs. 27 and 28, the obstructive effect of the net cage on the flow velocity is clearly observed. In most subplots of Figs. 27 and 28, the flow velocity remains relatively high after the wave passes through the floating platform without the net cage. However, when the net cage is present, the flow velocity decreases significantly compared to the case without the net cage. As the waves pass the front pontoon, the higher X-direction velocity within the waves leads to a Kármán vortex street-like flow behind the front pontoon, characterized by alternating high-speed flows on both sides of the front pontoon and a high-velocity region immediately behind it (Figs. 27 (5e), (6e) and Figs. 28(7d), (8d)). The presence of the net cage blocks this flow, thereby reducing the velocity behind the front pontoon. Additionally, there is a high-velocity region between the two side pontoons, which also decreases significantly when the net cage is present. Furthermore, as the flow speed increases, the obstructive effect of the

net cage on the flow becomes more pronounced.

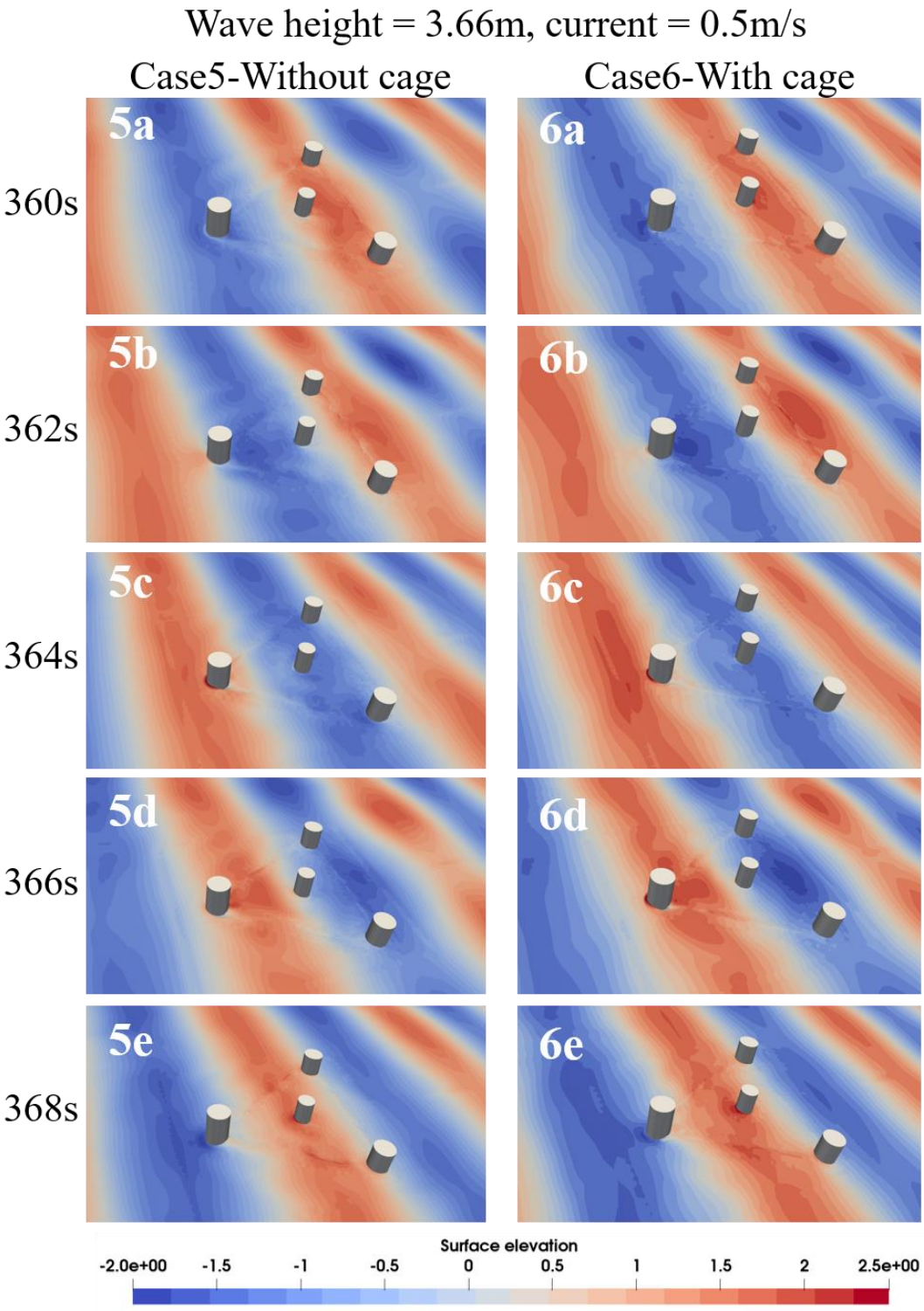

Fig. 25. Surface elevation in one cycle of cases 5 and 6.

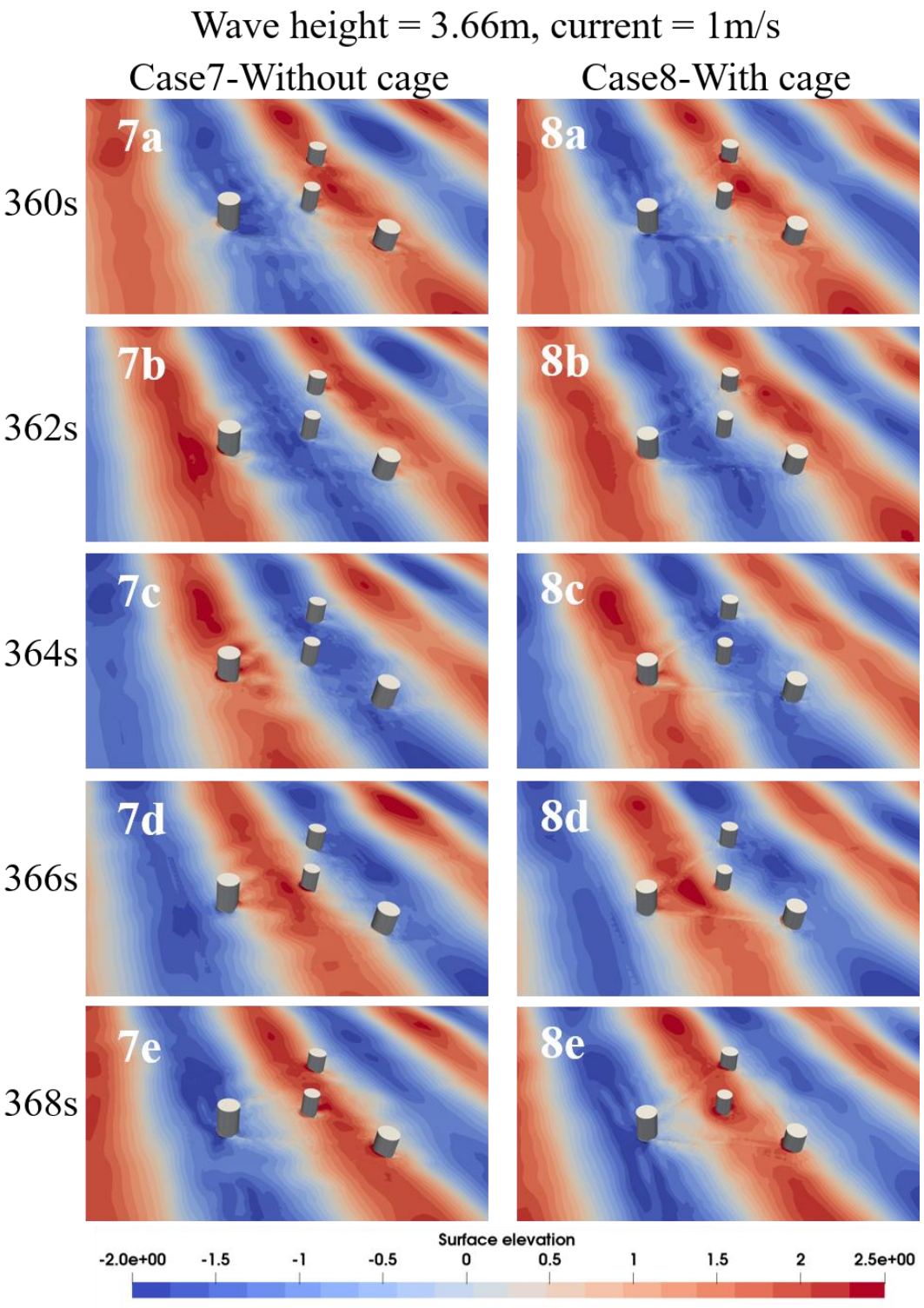

Fig. 26. Surface elevation in one cycle of cases 7 and 8.

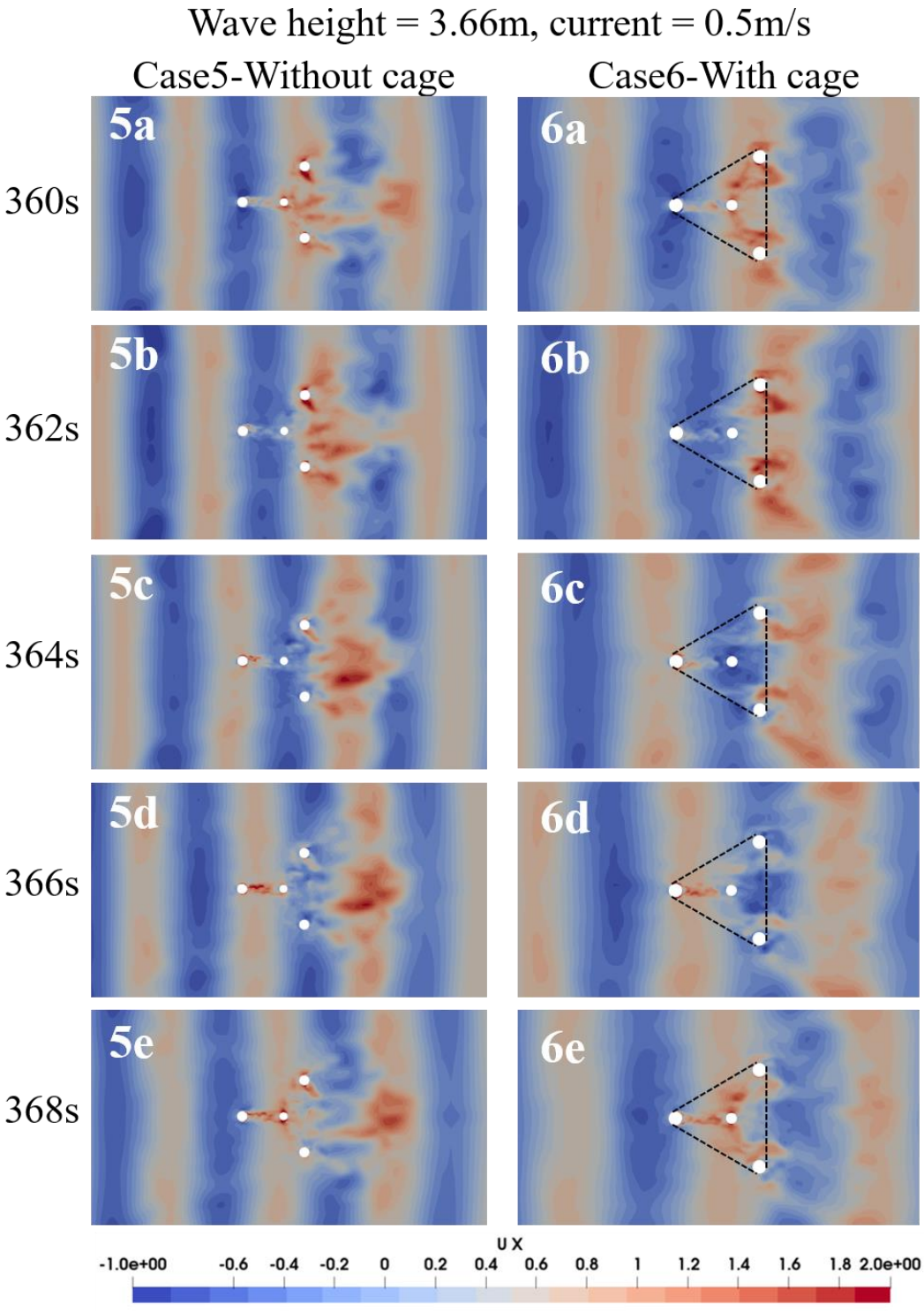

Fig. 27. Velocity in X direction within one cycle of cases 5 and 6.

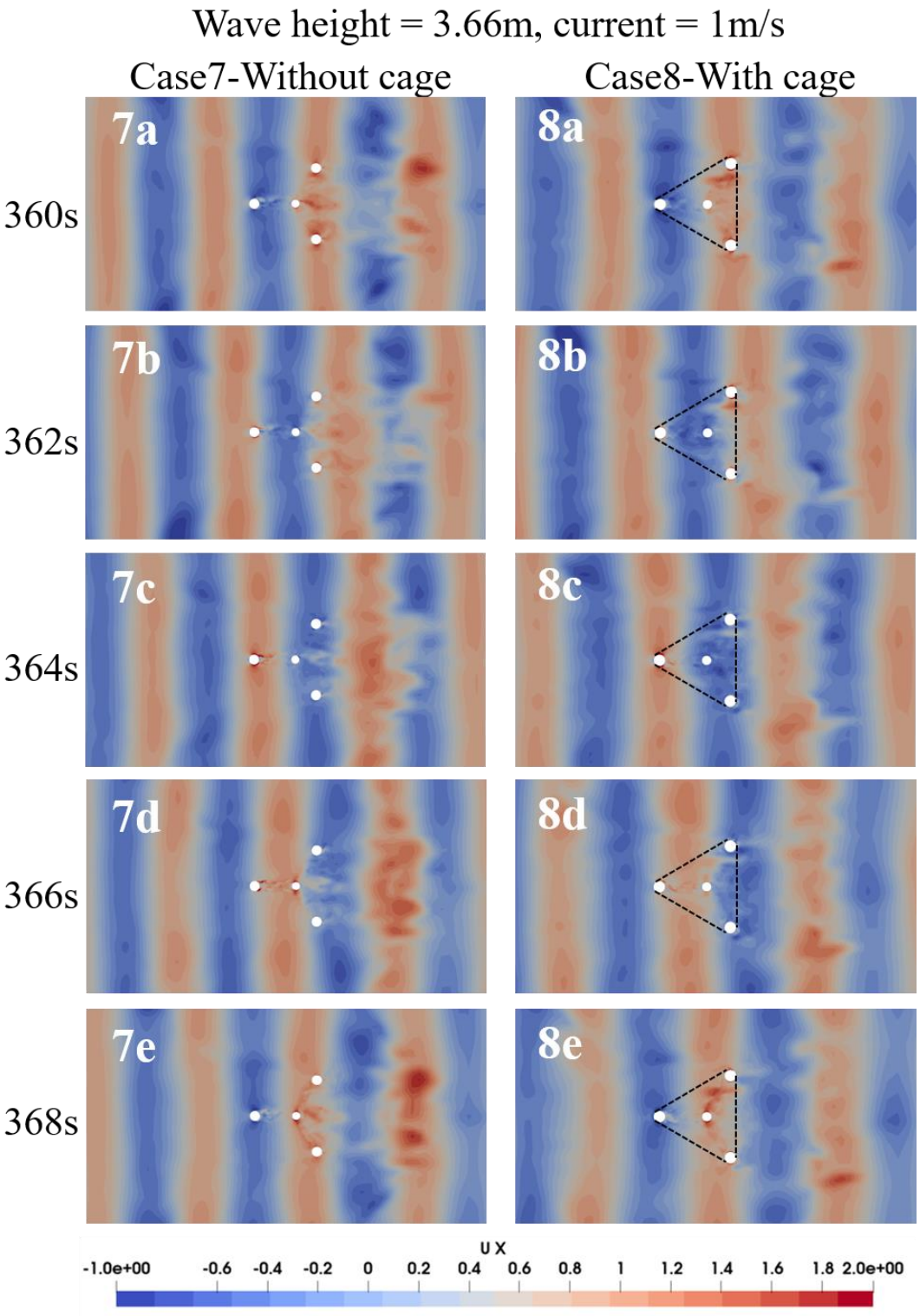

Fig. 28. Velocity in X direction within one cycle of cases 7 and 8.

6. Conclusion

This study developed a coupling solver, HybridMarineFoam, for the integrated structure of a FOWT and aquaculture net cage based on OpenFOAM, analyzing its aerodynamic, hydrodynamic and flow field characteristics.

Firstly, the presence of the net cage significantly increased the surge and pitch motion amplitudes of the integrated structure while slightly reducing the heave motion amplitude. And the net cage increased the mean surge position of the structure and decreased the mean pitch motion. Moreover, the net cage substantially increased the hydrodynamic load in the X-direction, which primarily caused the increased equilibrium position of the surge motion. As the flow velocity increased, both the time-mean value and the fluctuation amplitude of the net cage load in the x-direction also rose significantly. Furthermore, the net cage load is influenced by the velocities of both the flow field and the net cage motion. Vertically, the net cage motion velocity is mainly affected by the platform's heave and pitch motions; however, the pitch motion causes the two sides of the net to move in opposite directions. This complex net motion, combined with the flow field velocity, results in the net experiencing predominantly downward vertical loads. Additionally, due to the increased surge and pitch motion amplitudes caused by the net cage, the wind turbine thrust amplitude also increased significantly. Conversely, the presence of the net cage had minimal impact on wave height attenuation but exhibited a substantial obstructive effect on flow velocity. As waves passed by the front pontoon, a Kármán vortex street-like flow formed behind it, along with regions of high-speed flow. The net cage significantly weakened the

formation of this vortex street and reduced the X-direction flow velocity as the waves passed through it.

7. Future prospects

The currently developed HybridMarineFoam solver in this study includes only the wave, wind turbine, mooring and aquaculture cage modules. Our ongoing work focuses on developing an elasticity module to enable structural dynamic simulations of the blades and tower by considering aeroelastic effect, which will be expected to complete in the near future. Additionally, a control module will be developed for the wind turbine to achieve blade pitch and speed control, among others. In the future, we also plan to incorporate simulations of offshore photovoltaic and wave energy devices coupled with FOWTs.

Acknowledgements

This research work was financially supported by the National Natural Science Foundation of China, Grant No. is 51939002. Their financial supports are gratefully acknowledged.

Appendix A. OC4 semi-submersible NREL 5MW wind turbine

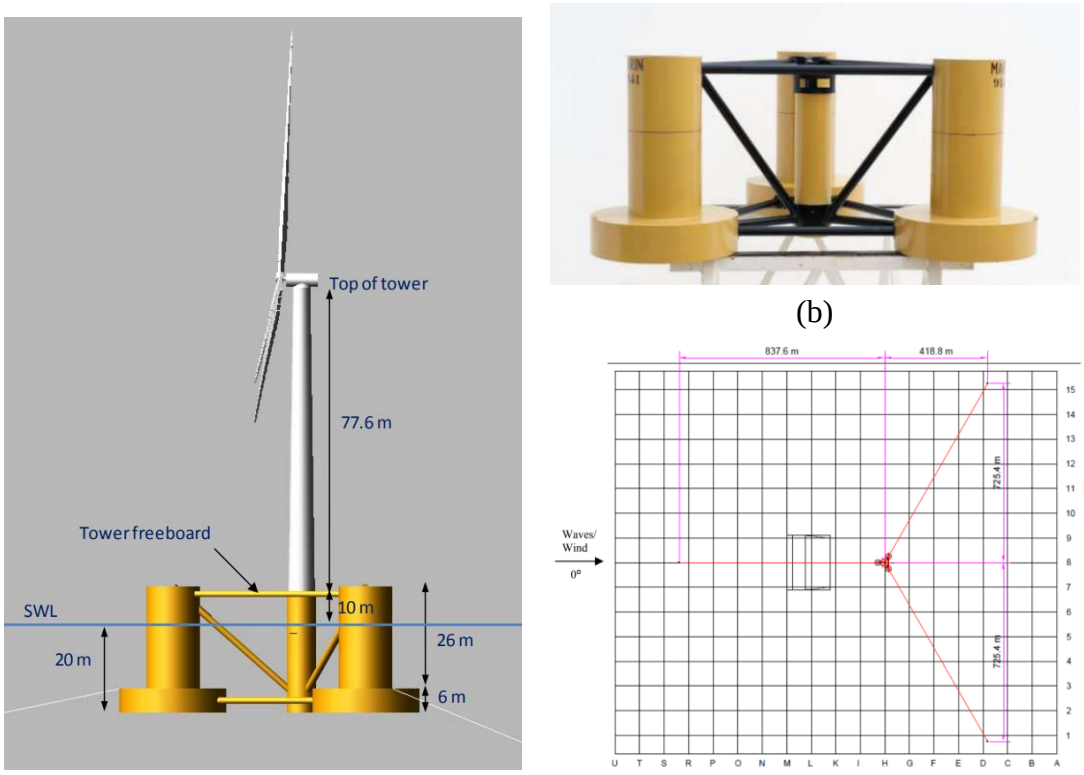

Fig. 29. Schematic of the NREL 5MW wind turbine mounted on the OC4 semi-submersible platform: (a) Sketch of the FOWT system; (b) DeepCWind OC4 platform; (c) Layout of the mooring system.

Table. 13 Gross properties of NREL 5 MW wind turbine.

FOWT	NREL 5MW
FOWT gross properties	
Total mass of the system	14,143,400 kg
CM location below SWL along platform centerline	10.20754 m
Platform roll inertia about CM	1.31657×10^{10} kg m^2
Platform pitch inertia about CM	1.31657×10^{10} kg m^2
Platform yaw inertia about platform centerline	1.90647×10^{10} kg m^2
Water depth	200 m
Mooring Line properties	
Number of mooring lines	3
Angle between adjacent lines	120°
Depth to anchors below SWL (water depth)	200 m
Depth to fairleads below SWL	14 m
Unstretched mooring line length	835.5 m
Mooring line diameter	0.0766 m

Equivalent mooring line mass in water	108.63 kg/m
Equivalent mooring line extensional stiffness	753.6 MN
Wind turbine properties	
Rotor configuration	3 blades
Rotor, hub diameter	126.0 m, 3.0 m
Overhang, shaft tilt angle and pre-cone angle of wind turbine	5 m, 5°, 2.5°
Hub height about SWL	90 m
Blade length	61.5 m
Cut in, rated, cut out wind speed	3, 11.4, 25 m/s
Cut in, rated rotor speed	6.9, 12.1 rpm

Note: SWL - still water level, CM - center of mass, rpm - revolutions per minute.

Appendix B. VolturnUS-S semi-submersible IEA 15 MW FOWT

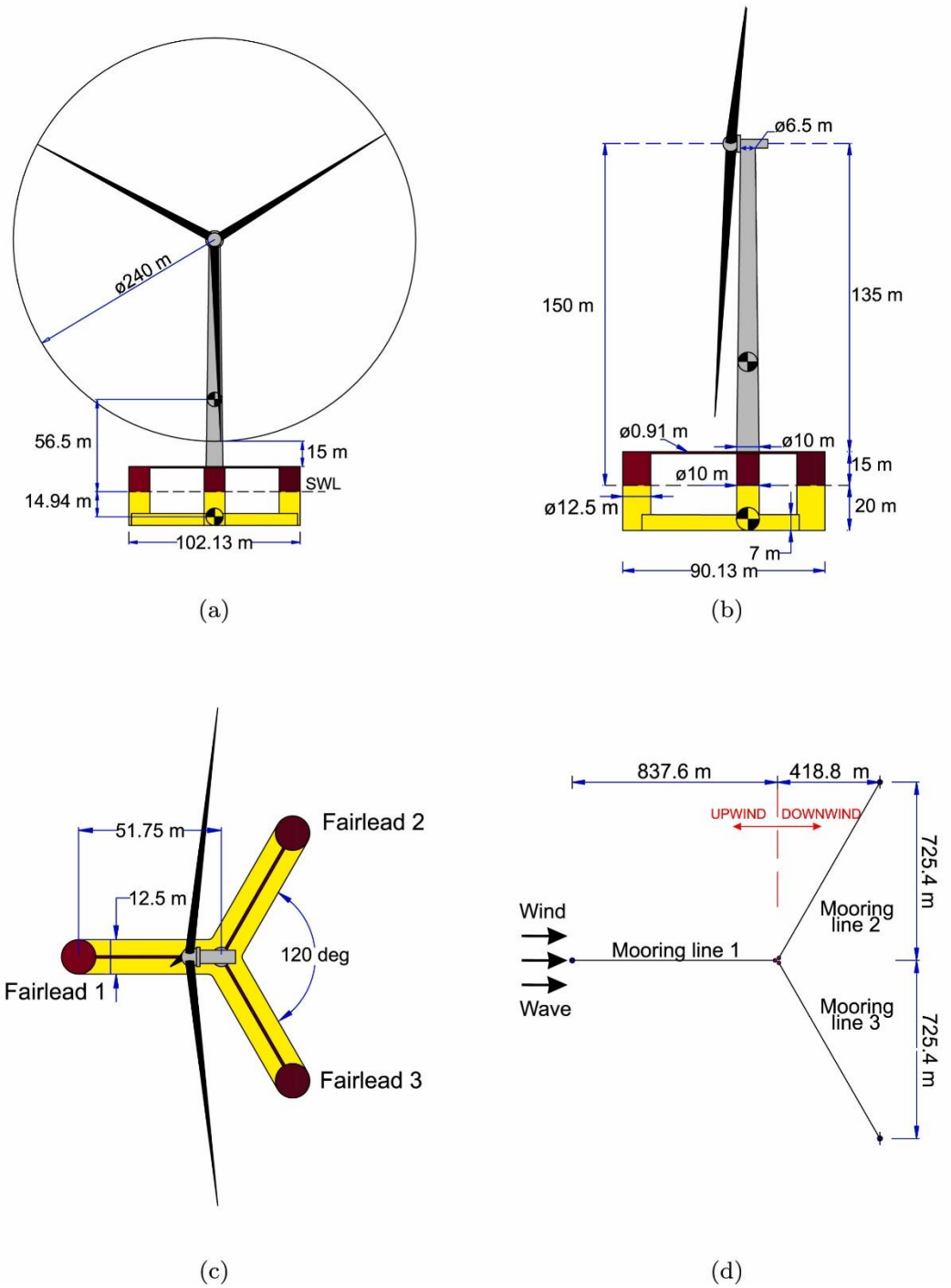

Fig. 30. Schematic of the IEA 15MW wind turbine mounted on the VolturnUS-S semi-submersible platform: (a) Front view; (b) Side view; (c) Top view; (d) Layout of the mooring system.

Table. 14 Gross properties of VolturnUS-S Semi-Subersible IEA 15 MW wind turbine.

FOWT	IEA 15MW
FOWT gross properties	
Total mass of the system	20,093,000 kg
CM location below SWL along platform centreline	2.04 m
Platform roll inertia about CM	4.396×10^{10} kg m^2
Platform pitch inertia about CM	4.386×10^{10} kg m^2
Platform yaw inertia about platform centreline	2.396×10^{10} kg m^2
Water depth	200 m
Mooring Line properties	
Number of mooring lines	3
Angle between adjacent lines	120°
Depth to anchors below SWL (water depth)	200 m
Depth to fairleads below SWL	14 m
Unstretched mooring line length	850 m
Mooring line diameter	0.185 m
Equivalent mooring line mass in water	685 kg/m
Equivalent mooring line extensional stiffness	3270
Wind turbine properties	
Rotor configuration	3 blades
Rotor, hub diameter	240.0 m, 7.94 m
Overhang, shaft tilt angle and pre-cone angle of wind turbine	11.35 m, 6°, 4°
Hub height about SWL	150 m
Blade length	117 m
Cut in, rated, cut out wind speed	3, 10.59, 25 m/s
Cut in, rated rotor speed	5.0, 7.56 rpm

Note: SWL - still water level, CM - centre of mass, rpm - revolutions per minute.

References:

Allen, C.A.V.H., 2020. Definition of the UMaine VolturnUS-S Reference Platform Developed for the IEA Wind 15-Megawatt Offshore Reference Wind Turbine. Golden, CO: National Renewable Energy Laboratory. NREL/TP-5000-76773..

Bi, C., Balash, C., Matsubara, S., Zhao, Y. and Dong, G., 2017. Effects of cylindrical cruciform patterns on fluid flow and drag as determined by CFD models. Ocean Eng. 135: 28-38.

Bi, C., Zhao, Y., Dong, G., Xu, T. and Gui, F., 2017. Numerical study on wave attenuation inside and around a square array of biofouled net cages. Aquacult. Eng. 78: 180-189.

Bui, C.M., Ho, T.X. and Khieu, L.H., 2020. Numerical study of a flow over and through offshore fish cages. Ocean Eng. 201: 107140.

Cai, Y., Zhao, H., Li, X. and Liu, Y., 2023a. Effects of yawed inflow and blade-tower interaction on the aerodynamic and wake characteristics of a horizontal-axis wind turbine. Energy, 264: 126246.

Cai, Y., Zhao, H., Li, X. and Liu, Y., 2023b. Aerodynamic analysis for different operating states of floating offshore wind turbine induced by pitching movement. Energy, 285: 129538.

Cai, Y., Li, X., Zhao, H., Shi, W., Wang, Z., Developing a multi-region coupled analysis method for floating offshore wind turbine based on OpenFOAM. Renew. Energy, 238:122026.

Cao, S., Cheng, Y., Duan, J. and Fan, X., 2022. Experimental investigation on the

dynamic response of an innovative semi-submersible floating wind turbine with aquaculture cages. Renew. Energy, 200: 1393-1415.

Chen, H. and Hall, M., 2022. CFD simulation of floating body motion with mooring dynamics: Coupling MoorDyn with OpenFOAM. Appl. Ocean Res. 124: 103210.

Chen, P., Kang, Y., Xu, S., Liu, L. and Cheng, Z., 2024. Numerical modeling and dynamic response analysis of an integrated semi-submersible floating wind and aquaculture system. Renew. Energy, 225: 120355.

Cheng, P., Huang, Y. and Wan, D., 2019. A numerical model for fully coupled aero-hydrodynamic analysis of floating offshore wind turbine. Ocean Eng. 173: 183-196.

Coulling, A.J., Goupee, A.J., Robertson, A.N., Jonkman, J.M. and Dagher, H.J., 2013. Validation of a FAST semi-submersible floating wind turbine numerical model with DeepCwind test data. J. Renew. Sustain. Ener. 5(2): 023116.

Devolder B, Rauwoens P, Troch P. Application of a buoyancy-modified k-ω SST turbulence model to simulate wave run-up around a monopile subjected to regular waves using OpenFOAM ®. Coast Eng 2017;125:81-94.

Devolder B, Troch P, Rauwoens P. Performance of a buoyancy-modified k-ω and k-ω SST turbulence model for simulating wave breaking under regular waves using OpenFOAM®. Coast Eng 2018;138:49-65.

Dong, S., You, X. and Hu, F., 2020. Effects of Design Factors on Drag Forces and Deformations on Marine Aquaculture Cages: A Parametric Study Based on Numerical Simulations. J. Mar. Sci. Eng. 8(2): 125.

Hu, Y., Zhao, H., Shi, W., Bi, C. and Li, X., 2023. Numerical Study on Internal and

External Flow Fields of the UHMWPE Cage. J. Mar. Sci. Eng. 11(10): 1881.

Huang, C., Tang, H. and Liu, J., 2007. Modeling volume deformation in gravity-type cages with distributed bottom weights or a rigid tube-sinker. Aquacult. Eng. 37(2): 144-157.

Huang, C., Tang, H. and Liu, J., 2008. Effects of waves and currents on gravity-type cages in the open sea. Aquacult. Eng. 38(2): 105-116.

Huang, Y., Cheng, P. and Wan, D., 2019. Numerical Analysis of a Floating Offshore Wind Turbine by Coupled Aero-Hydrodynamic Simulation. J. Mar. Sci. Appl. 18(1): 82-92.

Jacobsen, N.G., Fuhrman, D.R. and Fredsøe, J., 2012. A wave generation toolbox for the open‐source CFD library: OpenFoam®. Int. J. Numer. Methods Fluids 70(9): 1073-1088.

Jasak, H., 1996. Error analysis and estimation for the finite volume method with applications to fluid flows. Imperial College London (University of London).

Kristiansen, T. and Faltinsen, O.M., 2015. Experimental and numerical study of an aquaculture net cage with floater in waves and current. J. Fluids Struct. 54: 1-26.

Lei, Y., Zhao, S.X., Zheng, X.Y. and Li, W., 2020. Effects of Fish Nets on the Nonlinear Dynamic Performance of a Floating Offshore Wind Turbine Integrated with a Steel Fish Farming Cage. Int. J. Struct. Stab. Dyn. 20(03): 2050042.

Li, Z., Dong, G. and Yang, X., 2022. Onset of wake meandering for a floating offshore wind turbine under side-to-side motion. J. Fluid Mech. 934.

Limacher, E.D.L.P., 2022. On the relationship between turbine thrust and near-wake

velocity and vorticity. J. Fluid Mech. 949: A24.

Liu, Y., Xiao, Q., Ackermann, K., Peyrard, C. and Wan, D., 2017. Establishing a fully coupled CFD analysis tool for floating offshore wind turbines. Renew. Energy, 112: 280-301.

Lykke Andersen, T., Frigaard, P., Damsgaard, M.L. and De Vos, L., 2011. Wave run-up on slender piles in design conditions — Model tests and design rules for offshore wind. Coast. Eng. 58(4): 281-289.

Mao, X. and Sørensen, J.N., 2018. Far-wake meandering induced by atmospheric eddies in flow past a wind turbine. J. Fluid Mech. 846: 190-209.

Myrhaug, D. and Holmedal, L.E., 2010. Wave run-up on slender circular cylindrical foundations for offshore wind turbines in nonlinear random waves. Coast. Eng. 57(6): 567-574.

Patursson, Ø. et al., 2010. Development of a porous media model with application to flow through and around a net panel. Ocean Eng. 37(2-3): 314-324.

Pericàs, P.F., 2022. CFD Simulation of a Floating Wind Turbine in OpenFOAM: an FSI approach based on the actuator line and relaxation zone methods.

Ren, N., Li, Y. and Ou, J., 2014. Coupled wind-wave time domain analysis of floating offshore wind turbine based on Computational Fluid Dynamics method. J. Renew. Sustain. Energy, 6(2): 023106.

Shen, Y., Greco, M., Faltinsen, O.M. and Nygaard, I., 2018. Numerical and experimental investigations on mooring loads of a marine fish farm in waves and current. J. Fluids Struct. 79: 115-136.

Sørensen, J.N. and Shen, W.Z., 2002. Numerical Modeling of Wind Turbine Wakes. J. Fluids Eng. 124(2): 393-399.

Tran, T.T. and Kim, D., 2015. The coupled dynamic response computation for a semi-submersible platform of floating offshore wind turbine. J. Wind Eng. Ind. Aerodyn. 147: 104-119.

Tran, T.T. and Kim, D., 2016. Fully coupled aero-hydrodynamic analysis of a semi-submersible FOWT using a dynamic fluid body interaction approach. Renew. Energy, 92: 244-261.

Tran, T.T. and Kim, D., 2018. A CFD study of coupled aerodynamic-hydrodynamic loads on a semisubmersible floating offshore wind turbine. Wind Energy, 21(1): 70-85.

Wang, G., Martin, T., Huang, L., Bihs, H., 2022. Numerical investigation of the hydrodynamics of a submersible steel-frame offshore fish farm in regular waves using CFD. Ocean Eng. 256: 111528.

Wang, T. et al., 2023. Evolution mechanism of wind turbine wake structure in yawed condition by actuator line method and theoretical analysis. Energy Convers. Manag. 281: 116852.

Wang, T., Xu, T., Wang, S., Dong, G. and Yan, L., 2023. Hydrodynamic analysis of the combined structure of offshore monopile wind turbine foundation and aquaculture cage. Ocean Eng. 287: 115796.

Wang, Z. et al., 2024. Influence of tangential hydrodynamic force and inclination angle calculation on the dynamic responses analysis of mooring line based on lumped mass method. Ocean Coast. Manag. 255: 107247.

Yi, Y. et al., 2024. Experimental investigation into the dynamics and power coupling effects of floating semi-submersible wind turbine combined with point-absorber array and aquaculture cage. Energy, 296: 131220.

Yu, Z. et al., 2023. A hybrid numerical model for simulating aero-elastic-hydro-mooring-wake dynamic responses of floating offshore wind turbine. Ocean Eng. 268: 113050.

Zhai, Y., Zhao, H., Li, X. and Shi, W., 2022. Design and Dynamic Analysis of a Novel Large-Scale Barge-Type Floating Offshore Wind Turbine with Aquaculture Cage. J. Mar. Sci. Eng. 10(12): 1926.

Zhai, Y., Zhao, H., Li, X., Feng, M. and Zhou, Y., 2024. Effects of aquaculture cage and netting on dynamic responses of novel 10 MW barge-type floating offshore wind turbine. Ocean Eng. 295: 116896.

Zhang, C. et al., 2022. Modeling and dynamic response analysis of a submersible floating offshore wind turbine integrated with an aquaculture cage. Ocean Eng. 263: 112338.

Zhang, Y. et al., 2024. Experimental study on local scour for large-diameter mono-column composite bucket foundation for offshore wind turbines. Coast. Eng. 193: 104598.

Zhao, H., Hu, Y., Bi, C. and Li, X., 2024. Numerical study on hydrodynamic behaviors of and flow field around UHMWPE plane nets. Aquacult. Eng. 106: 102397.

Zhao, Y. et al., 2013. Numerical simulation of the flow field inside and around gravity cages. Aquacult. Eng. 52: 1-13.

Zhao, Z., Yu, W. and Xu, T., 2023. Study of the Interaction between Regular Waves and a Wind-Fish Combined Structure. Appl. Sci. 13(5): 3103.

Zhou, Y. et al., 2019. Numerical Modelling of Dynamic Responses of a Floating Offshore Wind Turbine Subject to Focused Waves. Energies (Basel), 12(18): 3482.

Zhou, Y. et al., 2022. Exploring inflow wind condition on floating offshore wind turbine aerodynamic characterisation and platform motion prediction using blade resolved CFD simulation. Renew. Energy, 182: 1060-1079.

Zhou, Y., Xiao, Q., Peyrard, C. and Pan, G., 2021. Assessing focused wave applicability on a coupled aero-hydro-mooring FOWT system using CFD approach. Ocean Eng. 240: 109987.

Zhu, X., Dong, G., Bi, C. and Zhao, Y., 2022. Wave diffraction of a hybrid wind turbine foundation with a double-layer aquaculture cage. Front. Mar. Sci. 9.